

1 Physical constraints on growth dynamics guide *C. elegans* developmental

2 trajectories and animal shape

3

4 Joy Nyaanga^{1,2}, Christina Goss³, Gaotian Zhang¹, Hannah N. Ahmed¹, Elliot J. Andersen¹, Isabella R.

5 Miller¹, Justine K. Rozenich¹, Iris L. Swarthout¹, Jordan A. Vaughn¹, Erik C. Andersen¹, Niall M.

6 Mangan³, and Sasha Shirman³

7

8 1. Department of Molecular Biosciences, Northwestern University, Evanston, IL 60208, USA

9 2. Interdisciplinary Biological Sciences Program, Northwestern University, Evanston, IL 60208, USA

10 3. Department of Engineering Sciences and Applied Mathematics, Northwestern University, Evanston, IL

11 60208, USA

12

13 **Keywords:** Developmental growth; growth control; *C. elegans*; feeding dynamics; growth dynamics; stretcher
14 model

15

16 **Acknowledgements:** We thank Jiping Wang and Keren Li for helpful advice about statistical data-analysis.

17 We would like to thank members of the Andersen laboratory and the Mangan group for their helpful comments
18 on the manuscript.

19

20 **Funding:** For this work, J.N., C.G., G.Z., E.C.A., N.M.M, and S.S. received support from the NSF-Simons
21 Center for Quantitative Biology at Northwestern University (awards Simons Foundation/SFARI 597491-RWC
22 and the National Science Foundation 1764421). C.G., S.S., and N.M.M. received support from the National
23 Science Foundation RTG: Interdisciplinary Training in Quantitative Biological Modeling, award 1547394). C.G.
24 was supported in part by the Murphy Scholars Program of the Robert R. McCormick School of Engineering and
25 Applied Science at Northwestern University.

26

27 **Competing interests:** The authors have no competing interests.

28

29 **Emails and ORCIDs:**

30 JN: JoyNyaanga2024@u.northwestern.edu, 0000-0002-1402-9213

31 CG: christinagoss2021@u.northwestern.edu, 0000-0002-5715-3337

32 GZ: gaotian.zhang@northwestern.edu, 0000-0001-6468-1341

33 HNA: hannahahmed02@gmail.com

34 EJA: elliotjandersen@gmail.com

35 IRM: miller.ir18@gmail.com

36 JKR: justine.rozenich@icloud.com

37 ILS: IrisSwarthout2023@u.northwestern.edu

38 JAV: JordanVaughn2023@u.northwestern.edu

39 ECA: erik.andersen@gmail.com, 0000-0003-0229-9651

40 NMM: niallmm@gmail.com, 0000-0002-3491-8341

41 SS: shirman.sasha@gmail.com, 0000-0001-5855-9470

42 Author contributions

- 43 **Conceptualization:** Joy Nyaanga, Gaotian Zhang, Christina Goss, Sasha Shirman, Niall M. Mangan, Erik C. Andersen
- 44 **Formal analysis:** Joy Nyaanga, Sasha Shirman
- 45 **Funding acquisition:** Erik C. Andersen, Niall M. Mangan
- 46 **Investigation:** Joy Nyaanga, Gaotian Zhang, Erik C. Andersen
- 47 **Manual image processing:** Joy Nyaanga, Hannah N. Ahmed, Elliot J. Andersen, Isabella R. Miller, Justine K. Rozenich, Iris L. Swarthout, Jordan A. Vaughn
- 48 **Methodology:** Joy Nyaanga, Gaotian Zhang, Christina Goss, Sasha Shirman
- 49 **Project Administration:** Erik C. Andersen, Niall M. Mangan
- 50 **Resources:** Erik C. Andersen
- 51 **Supervision:** Erik C. Andersen, Niall M. Mangan
- 52 **Validation:** Joy Nyaanga, Gaotian Zhang
- 53 **Visualization:** Joy Nyaanga, Sasha Shirman
- 54 **Writing - original draft:** Joy Nyaanga, Sasha Shirman, Christina Goss
- 55 **Writing - review & editing:** Joy Nyaanga, Sasha Shirman, Christina Goss, Gaotian Zhang, Erik C. Andersen, Niall M. Mangan

59 Abstract

60 Growth control is essential to establish organism size, so organisms must have mechanisms to both sense and
61 adjust growth. Studies of single cells have revealed that size homeostasis can be achieved using distinct
62 control methods: Sizer, Timer, and Adder. In multicellular organisms, mechanisms that regulate body size must
63 not only control single cell growth but also integrate it across organs and tissues during development to
64 generate adult size and shape. To investigate body size and growth control in metazoans, we can leverage the
65 roundworm *Caenorhabditis elegans* as a scalable and tractable model. We collected precise growth
66 measurements of thousands of individuals throughout larval development, measured feeding behavior to
67 pinpoint larval transitions, and quantified highly accurate changes in animal size and shape during
68 development. We find differences in the growth of animal length and width during larval transitions. Using a
69 combination of quantitative measurements and mathematical modeling, we present two physical mechanisms
70 by which *C. elegans* can control growth. First, constraints on cuticle stretch generate mechanical signals
71 through which animals sense body size and initiate larval-stage transitions. Second, mechanical control of food
72 intake drives growth rate within larval stages, but between stages, regulatory mechanisms influence growth.
73 These results suggest how physical constraints control developmental timing and growth rate in *C. elegans*.

74

75

76 Author summary

77 Precise growth control is essential to the development of proper adult body size and shape. Although a larger
78 body size can increase an organism's competitive advantage, an increased body size also requires added time
79 and nutrients to develop. As such, organisms must have mechanisms to both sense and adjust growth during
80 development. Studies of single cells have revealed that proper body size can be achieved using size or time
81 control mechanisms. In multicellular organisms, additional levels of control are required as growth must be
82 differentially regulated across cells, tissues, and organs. We leveraged the roundworm *Caenorhabditis elegans*
83 as a scalable model to investigate growth control in metazoans. As animals transitioned from one
84 developmental stage to the next, we observed changes in body shape while body size remained constant,

85 suggesting that animals might sense shape to set developmental timing. Two mechanisms likely control growth
86 rate, physical control of feeding rate and metabolic regulation, and we are able to identify developmental
87 periods where each govern growth. Our results demonstrate how physical constraints in tandem with other
88 regulation can be used to broadly control developmental timing and growth rate across diverse organisms.

89 Introduction

90 Growth is a complex process fundamental to development. Individual cells and whole animals must reach an
91 appropriate size to remain competitive in their environment. A larger body size conveys many selective
92 advantages to an organism, including increased predation success or defense against predation, increased
93 success in mating, and increased success in intraspecific as well as interspecific competition. Offsetting these
94 advantages, larger organisms require more food resources to grow, take longer to develop, and produce fewer
95 offspring [1]. Therefore, it is critical for multicellular organisms to effectively coordinate the growth of both
96 individual cells and the whole body. Additionally, growth at both of these scales must be coupled with
97 developmental progression to ensure the proper timing of irreversible developmental events.

98

99 In recent years, efforts have focused on understanding how organisms control growth to achieve size
100 homeostasis [2–4]. Many of these studies are motivated by the decades-long debate about whether growth is
101 linear or exponential; two separate models each having unique implications for size regulation. In a linear
102 model with constant growth rate, smaller organisms must grow proportionally more than larger organisms to
103 maintain size homeostasis. In this paradigm, organism size can be controlled simply by specifying growth
104 duration. Subsequently, this method of growth control is named the ‘Timer’ model [5,6]. Instead of regulating
105 growth duration, organisms can monitor size and adjust duration of growth to reach an optimal size, often
106 named the ‘Sizer’ model [7–9]. In an exponential model, growth rate is proportional to size. Here, a time-based
107 control mechanism alone would fail to maintain size homeostasis because larger organisms would grow
108 proportionally more during a specified period of time. This difference in growth requires a size-based control
109 mechanism to ensure that growth is halted once a maximum size is reached. Although ‘Timer’ and ‘Sizer’ are
110 the most often proposed size-control models, other models have been suggested, including ‘Adder’ in which a
111 fixed amount of material is added to a cell or organism during growth [10,11]. It is not trivial to determine which
112 model most accurately describes growth of individual cells or whole organisms because quantitative
113 measurements of growth must be collected at high precision and throughput under tightly controlled
114 experimental conditions. In unicellular organisms, the development of high-throughput experimental techniques

115 in combination with theoretical models have advanced the understanding of size control [12–16]. Progress has
116 been slower for multicellular organisms because cell growth within tissues and tissue growth within organisms
117 often progress at different rates, suggesting that they are likely not regulated in the same ways [17–19].

118

119 The nematode *Caenorhabditis elegans* presents both a scalable and tractable multicellular animal model to
120 study growth control. With an adult body length of approximately 1 mm, hundreds of thousands of individuals
121 are easily cultured in controlled laboratory conditions [20]. Moreover, *C. elegans* post-embryonic development
122 is marked by several molts that provide clear developmental milestones [21]. Each molt is initiated by a period
123 of inactivity (lethargus) and terminated once the animal successfully sheds its collagen-rich outer cuticle
124 (ecdysis) [22]. Four molts separate the *C. elegans* life cycle into five distinct stages: four larval stages (L1-L4)
125 and adult. The timing of these molts determines the completion of stage-specific development [23,24] and
126 underscores the importance of growth regulation during *C. elegans* larval development.

127

128 A full description of an organism's development includes the assessment of how growth and body size are
129 regulated. Initial studies of *C. elegans* development described whole-organism growth as a sigmoidal curve
130 characterized by continuous larval growth in length that reaches saturation in adulthood [25]. These early
131 studies hypothesized that molt events had little effect on continuous growth as the *C. elegans* cuticle allowed
132 for stretch during larval stages. Later work determined that larval progression was not continuous but rather
133 piecewise in nature [26]. This study showed that *C. elegans* volumetric growth rate increased from stage to
134 stage such that L1 animals had the slowest rate of growth and L4 animals had the fastest. This finding
135 suggests that *C. elegans* have a mechanism for regulating growth rate, potentially at each molt. Most recently,
136 researchers using single-animal imaging strategies observed that animals did not advance to the next
137 developmental stage until a critical volume was reached [27]. This finding suggests that *C. elegans* growth
138 follows a 'Sizer' model with each molt decision controlled by a volume threshold and further implies that
139 animals are able to communicate information about body size to precisely regulate growth.

140

141 Extensive characterization of *C. elegans* body size mutants has revealed several processes that influence
142 growth rate and body size [28]. A number of genes act through signaling pathways to influence growth and
143 body size [29,30]. Some of these pathways contribute to body size control by regulating cuticle collagen genes
144 [31]. Alternatively, mutations in some cuticle collagen genes directly disrupt the physical structure of the cuticle
145 [32]. These structural changes act as physical constraints on growth as opposed to regulatory mechanisms of
146 growth control. Environment factors also play a significant role in *C. elegans* growth control. Food restriction is
147 known to decrease growth rate or, when extreme, induce complete developmental arrest [27,33,34]. In *C.*
148 *elegans*, mutations that disrupt the ability to properly consume food also cause individuals to be small and thin,
149 indicating that food intake can act as a physical constraint on growth and body shape [35].

150

151 To understand *C. elegans* growth control at the whole-organism level, precise measurements of body size and
152 shape for large numbers of individuals are required. Using a combination of quantitative growth measurements
153 and mathematical modeling, we performed a high-resolution longitudinal study of *C. elegans* larval progression
154 and captured high-precision details about animal length, width, volume, and feeding dynamics. By investigating
155 *C. elegans* feeding and growth in tandem for thousands of individual animals, we found decreases in feeding
156 behavior associated with each larval transition that were also correlated in time with changes in growth. We
157 used our large-scale measurements of body size to further analyze the periods of time surrounding each larval
158 transition. At each molt, we observed simultaneous increases in length, decreases in width, and maintenance
159 of volume, suggesting that body shape in addition to size plays a role in the control of *C. elegans* growth.
160 Given these data, we propose a “Stretcher” mechanism for growth control whereby *C. elegans* senses body
161 size through physical constraints on cuticle stretch and undergoes larval-stage transitions when the cuticle
162 reaches its maximum capacity for stretch. Additionally, we propose that *C. elegans* are able to physically
163 constrain growth rate by the mechanical control of food intake. We used quantitative models of eating and
164 growth to evaluate our data and predicted that the rate of volumetric growth is primarily controlled by animal
165 feeding rate for most of development. However, at critical time points, including larval transitions, volumetric

166 growth rate was no longer primarily controlled by food intake and therefore other processes must control
167 resource allocation to influence growth.

168

169 Methods

170 Worm culture

171 The canonical laboratory strain N2 was obtained from the *C. elegans* Natural Diversity Resource [36]. Animals
172 were cultured at 20°C on 6 cm plates of modified nematode growth media (NGMA), which contained 1% agar
173 and 0.7% agarose seeded with *E. coli* OP50 bacteria [37].

174

175 Bacterial food

176 *E. coli* HB101 bacteria were prepared from cultures grown for 15 hours in Superbroth and then pelleted by
177 centrifugation. HB101 bacteria were diluted to OD100 in K medium (51 mM NaCl, 32 mM KCl, 3 mM CaCl₂,
178 and 3 mM MgSO₄ in distilled water) and stored at -80°C. Bacteria were thawed and fed to animals at a
179 concentration sufficient to sustain population growth from hatching to adulthood (OD20).

180

181 Growth of the animals

182 Populations of animals were propagated on NGMA plates for two generations without starvation. In the third
183 generation, gravid adults were bleach-synchronized [38]. Embryos were resuspended in K medium, aliquoted
184 into a 500 mL flask at a concentration of one embryo per μL, and allowed to hatch overnight. The following day,
185 arrested L1s were fed HB101 bacteria at a final concentration of OD20 in a final flask volume of 100 mL K
186 medium and HB101 food. Animals were grown for three days at 20°C with constant shaking. Following these
187 three days, adult animals were bleach-synchronized once more and embryos were aliquoted to seven replicate
188 500 mL flasks at a concentration of one embryo per μL in 100 mL. The following morning, six flasks were fed
189 HB101 bacterial food at a final concentration of OD20 in a final flask volume of 100 mL K medium and HB101
190 food. Two additional flasks were included to control for L1 animal size and possible clumping of bacterial food:
191 one flask contained L1 larvae but did not have food added and one flask contained no larvae but the same

192 concentration of HB101 bacteria as the six flasks containing L1 larvae. All replicate flasks were kept in an
193 incubator at 20°C with shaking for the duration of the experiment. A small temperature gradient of 1.25°C was
194 recorded in the shaking incubator with the highest temperature readings on the right side and lowest
195 temperature readings on the left side (S1 File). This slight variation in temperature contributed to variation in
196 developmental rate among replicates based on position within the incubator (replicates were placed in
197 numerical order with replicate 1 positioned on the far right side of the incubator).

198

199 **High-throughput measurements of body size and fluorescence**

200 Flasks were sampled each hour beginning one hour after feeding and continuing for 72 consecutive hours. At
201 each hour, 500 µL was removed from each flask and transferred to a well of a deep 96-well plate. Each flask
202 was sampled at each time point. Fluorescent polychromatic beads (Polysciences, 19507-5) with a 0.5 µm
203 particle size were added to each well at a final concentration of 3.64×10^8 beads/mL and incubated at 20°C for
204 10 minutes with shaking. Following the bead incubation, 30 µL from each well of the deep 96-well plate was
205 aliquoted to a 96-well microtiter plate. The process was repeated 11 times to 11 separate wells of the same
206 microtiter plate with pipetting to mix the well contents from the deep 96-well plate. Animals were then treated
207 with sodium azide at a final concentration of 50 mM to paralyze and prevent defecation of the ingested beads.
208 The 96-well plate was imaged with an ImageXpress Nano (Molecular Devices, SanJose, CA) at both 2x and
209 10x magnification. The ImageXpress Nano acquires brightfield images using a 4.7 megaPixel CMOS camera.
210 Images are stored in 16-bit TIFF format. Finally, animals were scored using a large-particle flow cytometer
211 (COPAS BIOSORT, Union Biometrica, Holliston MA). The COPAS BIOSORT sheath flow rate was kept at a
212 constant 10.3 ± 0.1 mL per minute to reduce variability in length measurements.

213

214 **Image processing**

215 Manual measurements of animal size were performed using the free Java image-processing program ImageJ
216 [39]. Well images for the six replicate flasks, excluding controls were loaded into ImageJ software. Length was
217 measured from head to tail, and width was measured at the widest point of the animal. Five animals were

218 measured per well across thirty total wells for each hour. Measurements were repeated for all 72 time points in
219 the assay. Body length and width were used to estimate animal area and volume by approximating the animal
220 as a cylinder. Pixels were converted to μm using a conversion factor of 3.2937 pixels/ μm .

221

222 Data processing

223 The COPAS BIOSORT was used to collect measurements of animal length (TOF), optical extinction (EXT),
224 and fluorescence for every animal in each well. These traits measure properties of nematode development
225 and, as such, increase as animals progress to adulthood [40]. Optical extinction measurements are the amount
226 of light absorbed over the full length of an animal as it passes through the instrument. An additional
227 measurement (norm.EXT) can be calculated by normalizing optical extinction by length. The raw data collected
228 were imported and processed using the *easysorter* R package [41].

229

230 The COPAS BIOSORT data were analyzed further using Gaussian finite mixture modeling as implemented in
231 the *mclust* R package [42]. These probabilistic models assume that data are generated from a mixture of
232 multivariate normal distributions and, therefore, can be used to classify unstructured data into meaningful
233 groups. Specifically, the *mclust* package fits a mixture model to data and selects the optimal number of clusters
234 using an expectation-maximization algorithm and Bayes Information Criteria. For model-based clustering, log
235 transformed animal length (logTOF) and log transformed optical extinction (logEXT) were used as inputs for
236 the *Mclust* function. Data from each hour of the experiment was analyzed by replicate and clusters that did not
237 appear to include majority animal objects were identified and removed as described previously [43]. This
238 processing removed non-animal objects such as bacterial clumps, shed cuticles, and next generation larval
239 animals from the time-course data.

240

241 We used a numpy polyfit regression of well-median data from the COPAS BIOSORT and image measurements
242 to convert TOF and norm.EXT data to microns (S5 File, Eq. S7-S9). Only the unit-corrected BIOSORT data
243 were used for further analysis.

244

245 Molt analysis

246 Fluorescence data obtained from the COPAS BIOSORT was used as a proxy for feeding behavior to
247 distinguish animals in a molt from growing animals. First, fluorescence was normalized by EXT to account for
248 the ability of larger animals to consume more food and beads. Next, an analysis of variance statistical model
249 was fit to the fluorescence data normalized by EXT to determine the amount of variance contributed by
250 replicate and well (Table S1). A local kernel regression smoothing method was then applied to the residuals of
251 the variance analysis using the *lokern* R package [44]. Residuals were used to address only the differences
252 over time and ignore minor variation among replicates and wells. The local minima of the regression function
253 were found by solving for where the first derivative of this function equaled zero. The time associated with each
254 local minimum was used to represent the timing of each molt. Molts occurred at 14, 25, 36, and 48 hours.
255

255

256 To identify periods of time that contained a majority of growing animals, the inflection points of the regression
257 function were calculated by solving for where the second derivative of the function equaled zero. Time points
258 between inflection points that did not contain a local fluorescence minimum were considered as growth
259 periods. These hours were 1-13, 17-22, 27-32, and 39-45 corresponding to L1, L2, L3, and L4 growth periods.
260

261 Each molt is initiated when animals enter lethargus: a behavioral state where animals cease active feeding. To
262 classify individual animals as in a molt or growing, we set a quiescence threshold using fluorescence
263 measurements at each local minimum. The fluorescence measurement at each local minimum was as follows:
264 0.07, 0.06, 0.06, 0.06. The average of these measurements (0.06) was used as the fluorescence threshold
265 signifying quiescent behavior. Any individual animals that fell below this threshold fluorescence value were
266 designated as in a molt and animals above this threshold value were classified as growing.

267

268 Comparison of model fits

269 To determine the volume growth model, we fit linear, exponential, and cubic functions to data designated as
270 growth periods for each larval stage. Both linear and nonlinear functions were fitted using least-squares
271 regression. Akaike's information criterion (AIC) [45] and Bayesian information criterion (BIC) [46] were
272 goodness of fit criteria used to evaluate candidate models. To assess the strength of evidence for each
273 candidate model, we identified the model with the smallest AIC/BIC value and assessed the difference
274 between this value and the AIC/BIC of the other two models. The magnitude of the difference was used to
275 determine the level of support for each candidate model as previously described [47,48]. All model fits and
276 analysis were performed using the *stats* R package.

277

278 Stretcher and feeding model analysis

279 To analyze shape dynamics, length and width data from growth time periods were extracted from the full
280 COPAS BIOSORT population data and analyzed from each replicate separately to avoid issues with replicate
281 variability. For replicate 2, the hours defining growth periods were 1-13, 16.37-22.39, and 26.93-32.96;
282 corresponding to L1, L2, and L3. Hours defining larval stages were rounded as data was collected at exact
283 hour increments. The L4 stage was excluded from the analysis because of the high variability within the
284 population. We applied a local kernel regression, *lokern* R package [49], to smooth the population dynamics of
285 length and width. To calculate mean and standard deviation, the smoothed population measurements were
286 bootstrapped using 2,000 samples with replacement (S5 File, Algorithm S1). To determine cuticle properties
287 throughout larval stages, we calculated the mean ratio of derivatives of regression width and length. Error for
288 this ratio was calculated using error propagation to pass the bootstrap variation through the ratio (S5 File, Eq.
289 S24-28).

290

291 To analyze volumetric growth dynamics and feeding dynamics, volume regression was calculated using a
292 cylindrical approximation for animal shape (S5 File, Eq. S7-S9) and the same local kernel regression
293 previously described was applied to red fluorescence data. Volume growth rate was calculated using the

294 python numpy gradient function applied to the volume regressions. An additional moving time window average
295 (1.4 hours) was applied to smooth numerical errors in the derivative when determining feeding and growth
296 regime transition points (S13 Fig).

297

298 **Data availability**

299 The authors state that all data necessary to confirm the conclusions of this work are within the text, figures,
300 and supporting information files. All files and code for analysis and generation of figures and tables present
301 within the article are archived on GitHub (<https://github.com/AndersenLab/C.elegans-growth-manuscript>).

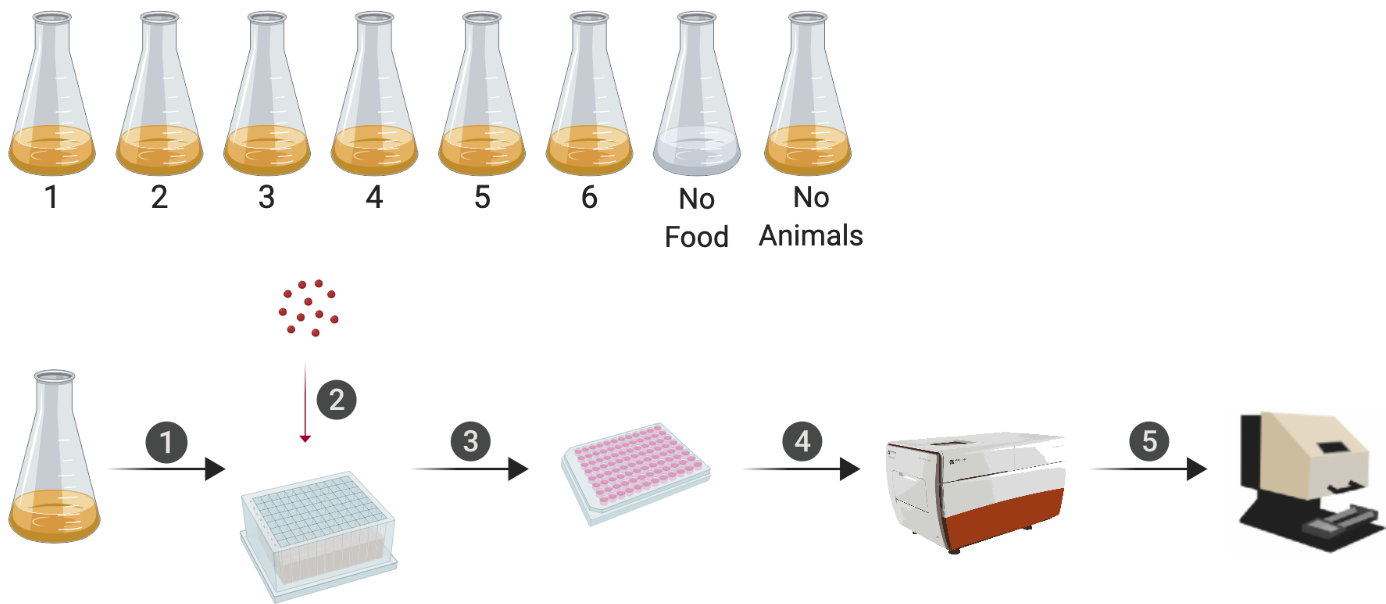
302

303 **Results**

304 **Quantitative measurements of *C. elegans* growth**

305 We have optimized a quantitative growth assay that reliably measures small changes in *C. elegans* body size
306 throughout development (Fig 1). Our method provides both high-throughput and high-precision assessment of
307 developmental growth. In brief, populations of 100,000 animals were cultured in flasks. Every hour after
308 feeding, a sample of the population from each flask (~300 animals/flask) was collected to measure animal
309 length, width, and feeding rate. The ImageExpress imaging system was used to collect images of sampled
310 animals. Feeding rate, examined using fluorescent microspheres, and body size were then measured using the
311 COPAS BIOSORT. The imaging platform allowed for the further analysis of life stage and body size,
312 contributing added precision to our measurements. We cultured six replicate populations of *C. elegans* for a
313 total of 600,000 synchronized and growing animals. We sampled approximately 2,000 individuals each hour,
314 generating highly scaled data to further assess *C. elegans* growth dynamics.

315



318 Schematic of the experimental workflow is shown. Synchronized animals were cultured in flasks where six
319 flasks contained replicate populations of nematodes, one flask had a population of unfed animals, and one
320 flask only contained bacterial food. At each hour of the experiment, all eight flasks were sampled. In step 1,
321 animals were transferred from each flask to a single well of a 96-well microtiter plate. In step 2, fluorescent
322 beads were added to each well. Following a 10-minute incubation period, animals from each well of the
323 deep-well plate were transferred to several wells of a 96-well microtiter plate for step 3. In step 4, animals in
324 each well of the microtiter plate were imaged. In step 5, the same animals were measured using the COPAS
325 BIOSORT. This process was repeated every hour after feeding for 72 consecutive hours (see Methods).

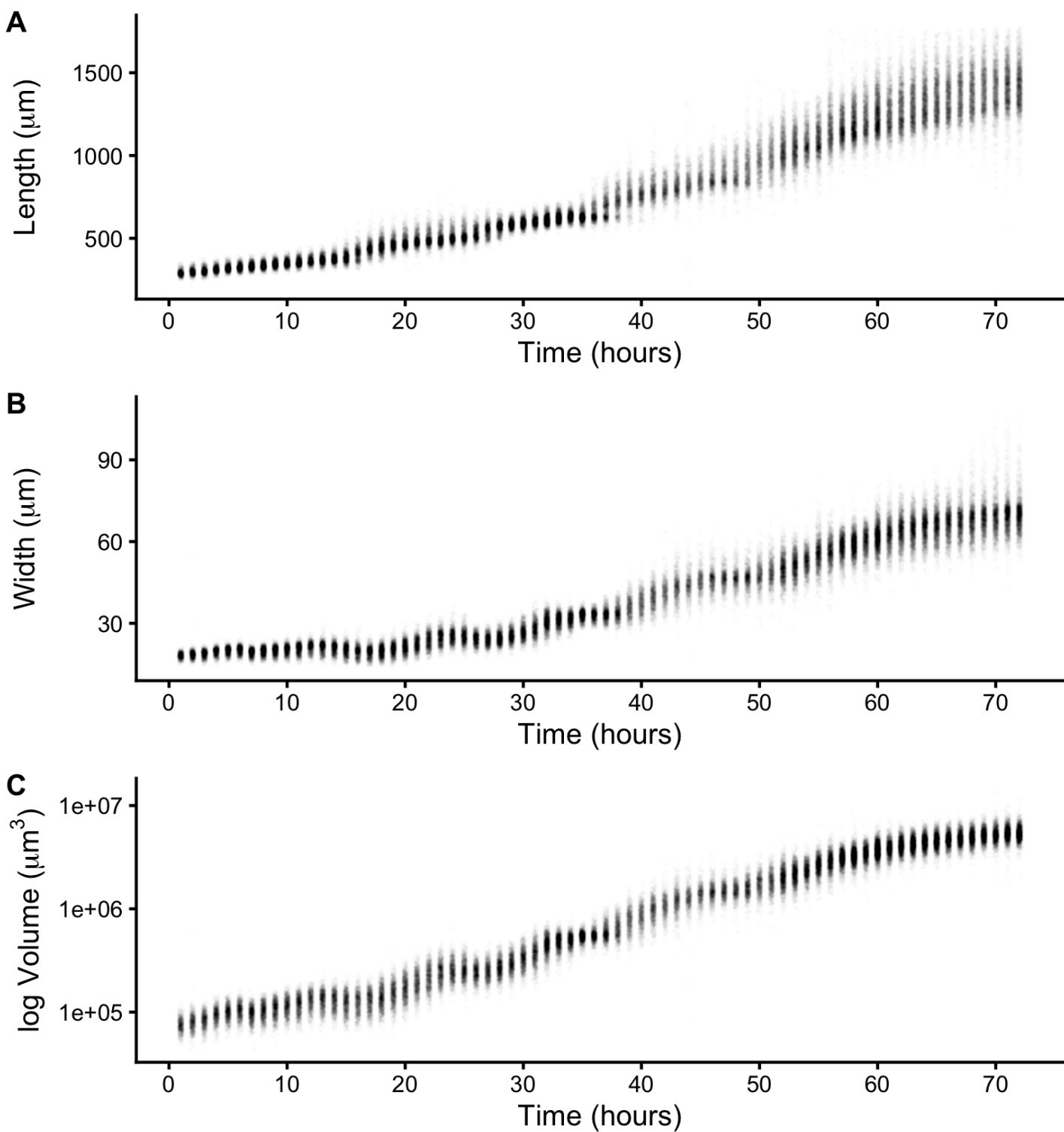
326

327 The raw data from the quantitative growth assay provides measurements of body size and feeding behavior,
328 which are traits related to animal growth. Two measurements of body size were collected from raw data taken
329 from the COPAS BIOSORT: time of flight (TOF) and optical extinction (EXT) (S1 Fig). Time of flight is a
330 measurement of body length, and optical extinction is influenced by body length, thickness, and composition
331 [40]. We investigated whether optical extinction could be correlated to a different measure of body size,
332 through the collection of manual size measurements from images (see Methods). We calculated the median
333 length, width, area, and volume of animals in a subset of imaged wells from each hour of the experiment. We

334 then compared these values to well median statistics from the processed COPAS BIOSORT data. We found a
335 strong correlation between manual measurements of animal length from the image analysis and TOF
336 measurements from the COPAS BIOSORT. We also observed an equally strong correlation between manual
337 measurements of animal area and EXT as well as animal width and EXT normalized by body length
338 (norm.EXT) (S2 Fig). We then approximated animal volume using measurements from the COPAS BIOSORT
339 by using a cylindrical approximation for *C. elegans* shape (see Methods). This result expanded the number of
340 body size parameters that we were able to assess using the COPAS BIOSORT data, allowing us to investigate
341 growth dynamics in length, width, and volume (Fig 2A-C). To disentangle nematode objects from non-animal
342 objects (bacteria clumps, detritus, shed cuticles), we employed model-based clustering to remove unwanted
343 objects from analysis and better examine growth of animals (S3 Fig). Lastly, we converted COPAS BIOSORT
344 measurements into microns (see Methods).

345

346



347 **Fig 2. Quantitative measurements of animal size.**

348 COPAS BIOSORT data of animal length (A), width (B), and volume (C) after the removal of non-animal objects

349 using model-based clustering methods (see Methods).

350

351 We report body length, width, and volume of animals at each hour of development from L1 to adult (S1 Fig and
352 Fig 2). Historically, growth of *C. elegans* has been shown as a sigmoidal curve where exponential growth
353 during larval stages reaches a maximum rate in adulthood [25]. More recently, researchers have identified that
354 growth curves are discontinuous during development punctuated by larval transitions [26,27]. Using our
355 quantitative growth assay, we captured these small-scale discontinuities in larval growth as well as an apparent
356 growth maximum during early adulthood. We noticed that all size variables (length, width, and volume)
357 displayed these dynamics. Objects identified as animals appear to grow in size. However, in particular time
358 windows during development, growth dynamics visibly shift, producing discontinuities in animal size. With
359 these data, we were able to further investigate *C. elegans* growth and size control.

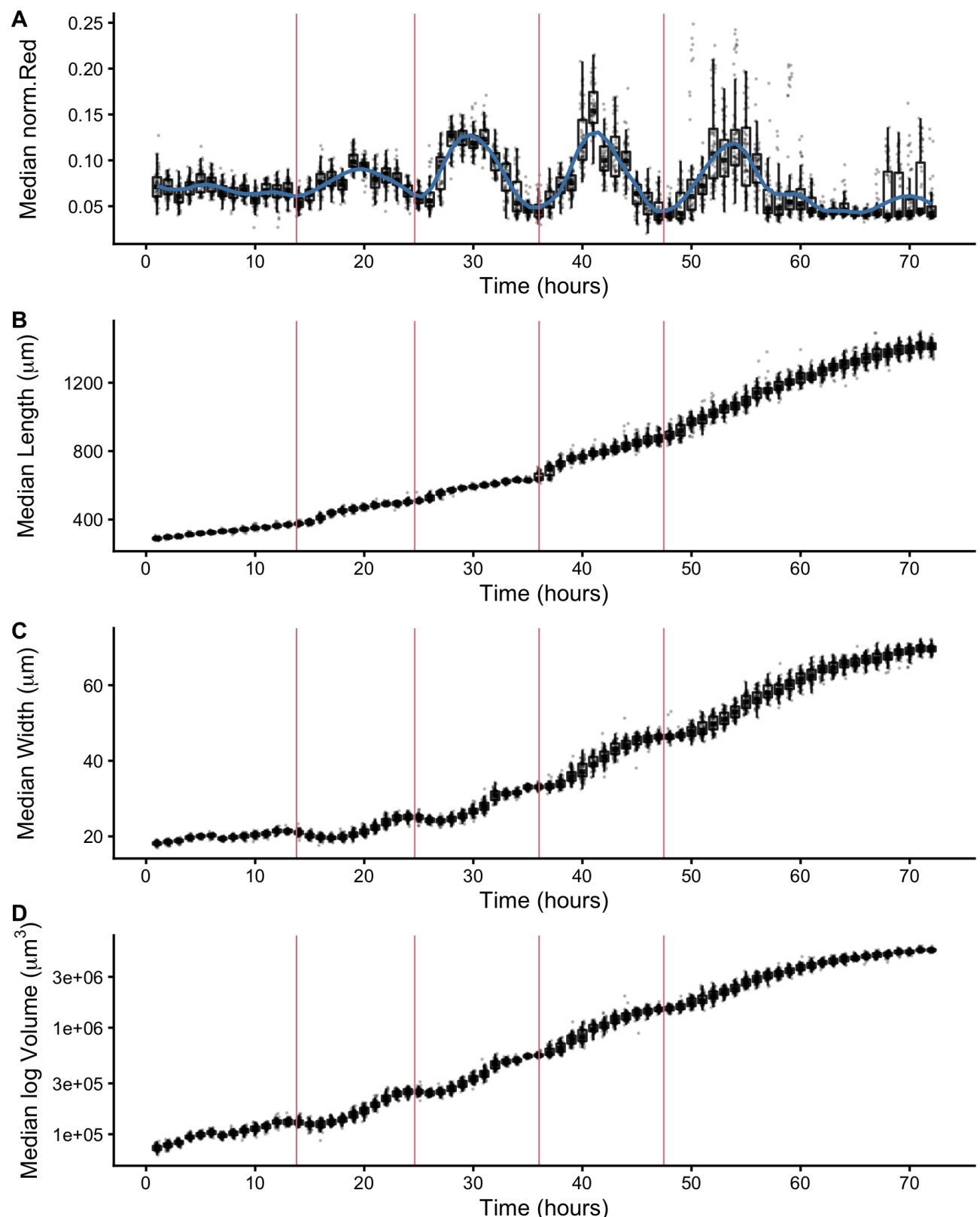
360

361 **Fluorescence provides a quantitative measurement of animal feeding behavior and
362 developmental progression**

363 In addition to body size and shape, the raw data from the quantitative growth assay described above measured
364 fluorescence of each animal object. To readily assess the thousands of measurements acquired at each hour,
365 we generated summary statistics of median well measurements (S1 Table). With these summarized data, we
366 investigated the relationship between feeding behavior and developmental stage. It is well established that
367 temporary suspensions of *C. elegans* feeding occur during each molt [25,50]. As such, active feeding is
368 frequently used to distinguish growing animals from individuals in a molt. We quantified feeding behavior by
369 exposing animals to fluorescent beads the approximate size of bacteria and measuring fluorescence of
370 animals [51]. Because larger animals are able to consume more food and therefore contain more ingested
371 food, we normalized fluorescence by animal area to account for increases in body size (S4 Fig). The resulting
372 fluorescence data showed a dynamic pattern (Fig 3A). At approximately 15 hours, fluorescence steadily
373 increased to a peak before decreasing back to initial levels at approximately hour 27. This pattern, repeated
374 three additional times, established clear time windows of local minimal fluorescence. These local minima
375 represent periods of time where a large proportion of the population had reduced or ceased feeding and
376 therefore suggests time windows where a majority of animals were likely not feeding because they were in a

377 molt. We used a local kernel regression method to estimate a smooth curve and calculate the derivative to
378 identify the time associated with each local minimum (see Methods). We then assessed images collected from
379 the growth assay and demonstrated that periods of decreased feeding are concurrent with the presence of
380 shed cuticles, supporting that animals are undergoing a molt during these periods of time (S5 Fig). When we
381 overlaid the timing of each local minimum on the population size data, we were able to outline the start and
382 end of each larval stage (Fig 3B-D). Notably, local minima occur approximately every ten hours, consistent with
383 well established observations of molt timing [25]. Furthermore, we observed a clear relationship between
384 changes in feeding behavior and growth dynamics where decreases in feeding occurred simultaneously with
385 discontinuous growth in length, width, and volume.

386



388 Fig 3. Fluorescence dynamics outline larval stages.

389 (A) Median normalized red fluorescence (y-axis) over time (x-axis) is shown. The blue line represents the
390 kernel regression fit to the data. The red vertical lines correspond to the local minima of the regression and
391 represent the transition between larval stages. Median length (B), median width (C), and median log volume
392 (D) are shown with larval-stage transitions as well.

393

394

395 **Changes in *C. elegans* body shape occur at larval-stage transitions**

396 Adult body size is ultimately determined by the coordination of developmental progression and rate of growth.
397 To understand how *C. elegans* achieve final size, we must first examine how *C. elegans* grow. Quantitative
398 studies of *C. elegans* growth frequently assess changes in length or volume over time; however, to fully
399 characterize changes associated with growth, it is also important to consider the dynamics of width. Two
400 general models were proposed for *C. elegans* growth in volume: linear and exponential [25–27]. It is important
401 to note that these volume growth models require different dynamics in length and width. To achieve linear
402 volume growth, length and width must increase at precise sublinear rates that together result in a linear
403 increase in volume. If animal length and width increased at a constant linear rate, then volume would increase
404 at a cubic rate. Alternatively, if both length and width grew exponentially, then volume would fit an exponential
405 model. We sought to identify which model best described *C. elegans* growth behavior but were unable to
406 consistently distinguish between linear, exponential, and cubic models using statistical information criterion
407 because of the similarity in the shapes of the growth curves (S6 Fig and S2 Table). This result is not surprising
408 because computational simulations have shown that increases in experimental noise, above 2% added noise,
409 limit the correct identification of growth models [52].

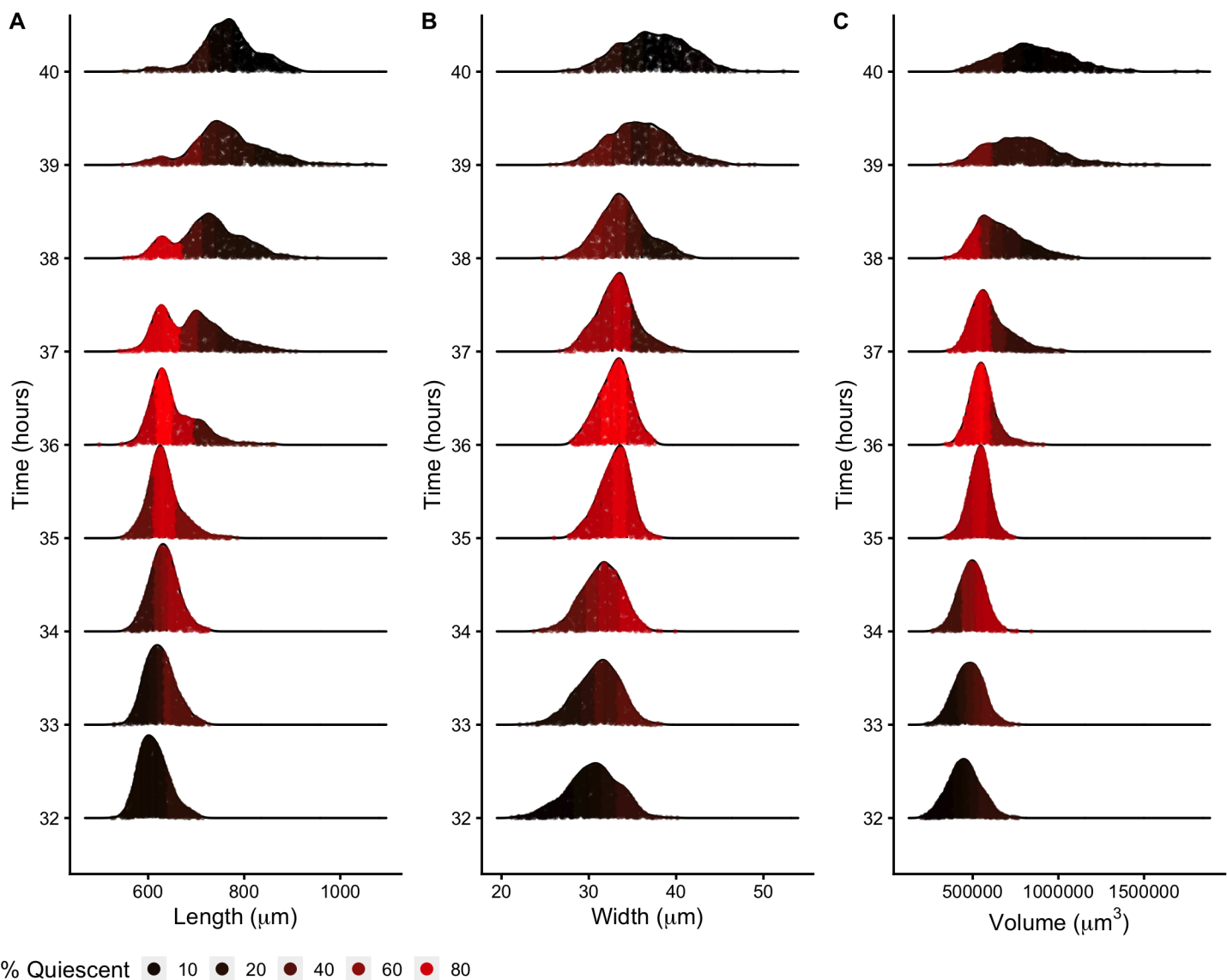
410

411 Growth has important implications for how animals regulate size. Size homeostasis requires that growth rate
412 and developmental rate are coordinated. *C. elegans* reach a similar volume at each larval transition despite
413 significant variation in individual growth rates [27]. Because individuals in a population maintain similar sizes
414 despite differences in growth rate, a control mechanism to regulate developmental progression must exist.

415 Previous studies proposed a size-based growth control model in *C. elegans* where animals must reach a
416 threshold size before advancing to the next developmental stage [27]. To assess changes in body size and
417 shape during a larval transition, we examined the dynamics of animal length, width, and volume in the hours
418 before, during, and after each molt. We find that for each shape variable, larger animals enter molt first (Fig 4).
419 We also observe differences in the distributions of lengths during a larval transition compared to widths and
420 volumes. Measurements of animal width and volume remain unimodal throughout a molt, but length does not.
421 As larger animals begin to exit the molt, an increase in body length occurs that leads to the appearance of
422 bimodality of lengths across the population. This length increase occurs simultaneously with a decrease in
423 widths across the population. Importantly, volume remains constant while length increases and width
424 decreases, indicating a change in body geometry not size (Fig 3 and Fig 4). These changes in the physical
425 dimensions at each larval transition suggests that body shape, in addition to size, is involved in the control of
426 *C. elegans* growth.

427

428



429 **Fig 4. Density plots of population size dynamics during a single larval transition.**

430 Population density curves of length (A), width (B) and volume (C) for the hours surrounding the L3 - L4 larval
431 transition. Each distribution was divided into five quantiles. The percentage of quiescent animals present within
432 each quantile was calculated (see Methods), and each quantile was colored to reflect this percentage. In all
433 shape variables, quantiles that contain the largest animals displayed an increase in quiescence earlier than
434 quantiles that contain the smallest animals. These dynamics were consistent across all larval-stage transitions
435 (S7 Fig).

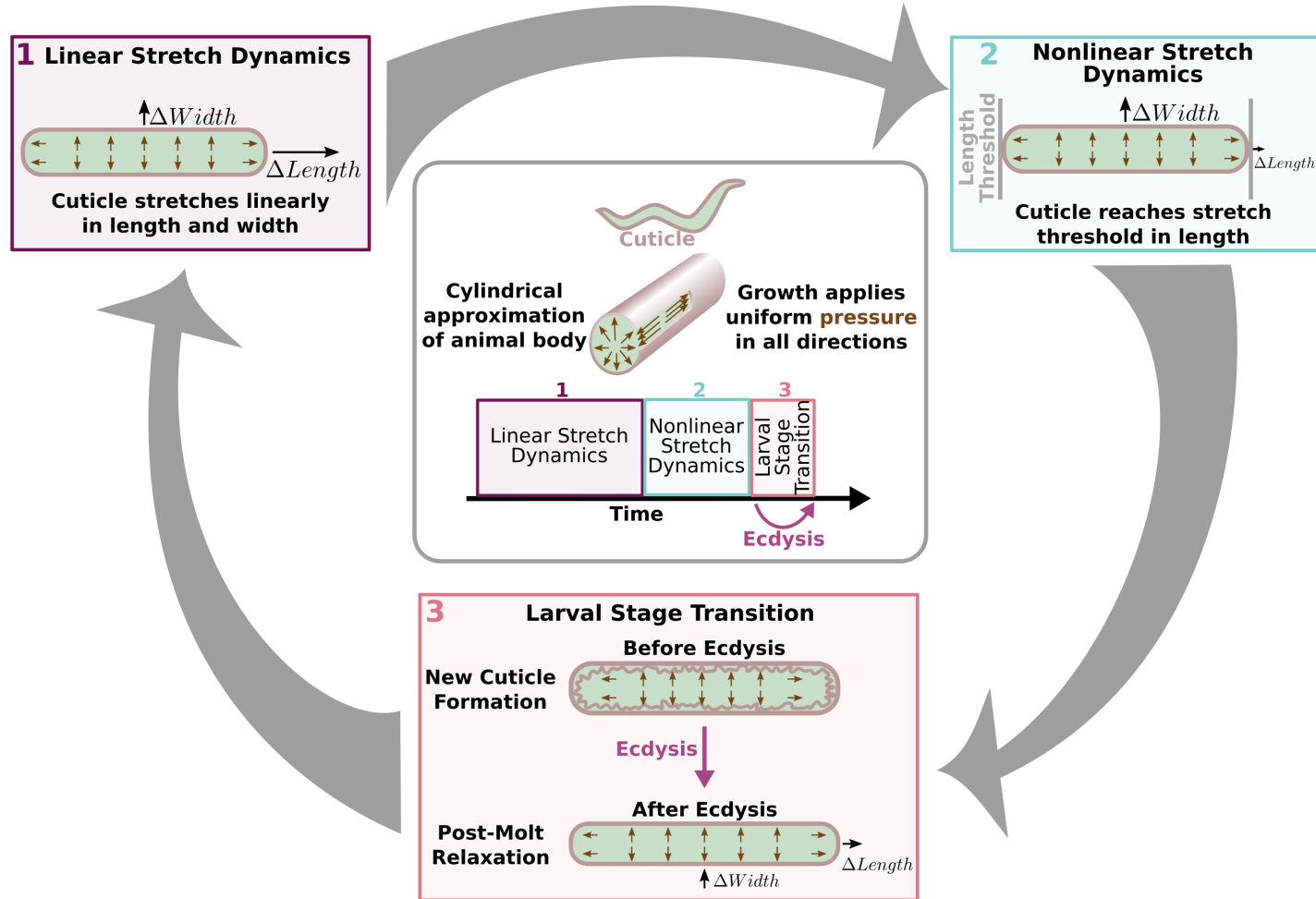
436

437 Cuticle stretch determines timing of larval-stage transitions

438 Previous studies theorized that the internal mechanism for sensing body size and triggering molts in *C. elegans* is driven, in part, by the properties of the collagen-rich cuticle [27]. Many cuticle collagen mutations
439 cause morphological defects in nematode shape some of which cause animals to be shorter but do not impact
440 animal width, implying that the cuticle affects length and width independently [53]. The *C. elegans* cuticle does
441 not grow through the addition of new material, but rather stretches to accommodate increases in animal body
442 size. Cuticle stretch is limited by the material properties of the cuticle. Previous work on *nekl-3(sv3)* mutants
443 demonstrated that the cuticle can become sufficiently stiff to restrict *C. elegans* growth after a period of
444 stretching [54]. These mutants are unable to shed the cuticle around the middle part of their body, restricting
445 the size of the encased middle to pre-molt dimensions while the head and tail continue to grow normally. We
446 hypothesize that *C. elegans* sense when the cuticle becomes restrictive and use a threshold in the reduction of
447 elasticity or “stretchiness” of the cuticle to determine when to initiate molt.
448

449

450 To explain the initialization of molt behavior, we developed a “Stretcher” model for a cuticle-stretch-based
451 threshold that triggers *C. elegans* larval-stage transitions. We propose that the nematode passes through three
452 distinct regimes related to cuticle stretch: linear stretch dynamics, non-linear stretch dynamics, and larval stage
453 transition (Fig 5). The cuticle structure is anisotropic, possibly leading to distinct properties in the length and
454 width directions [55,56]. We approximated the cuticle as a hollow cylinder of negligible thickness filled by the
455 body of the nematode. Growth is modelled as internal pressure evenly applied to the cuticle in all directions.
456 The cuticle responds differently during linear stretch, nonlinear stretch, and post-molt relaxation.
457



459 **Fig 5. Cuticle stretch determines larval-stage transitions**

460 The “Stretcher” model describes each larval stage as a cycle. Nematodes are modeled as a cylindrical object
461 with a thin cuticle epidermis. (Box 1) Linear Stretch Dynamics: uniform growth pressure stretches the cuticle
462 linearly in both length and width. (Box 2) Nonlinear Stretch Dynamics: Cuticle has reached a stretch threshold
463 in length, and under uniform growth pressure the length stretches less (sub-linear) and width stretches linearly.
464 (Box 3) Larval Stage Transition: a new cuticle is formed and the old cuticle is shed (ecdysis), removing
465 constraints in length. The nematode body “relaxes” in length, causing an increase in length, a decrease in
466 width, and constant volume.

467

468 In the linear stretch regime (Fig 5), the cuticle is linearly elastic in both the length and width directions,
469 stretching proportionally to the pressure exerted on the cuticle. Previous work found evidence for a linearly

470 elastic cuticle [57,58] in animals expanded in a negative external pressure environment or after positive force
471 was applied to the cuticle. A linearly elastic cuticle will have ΔL stretch in the length direction and ΔW stretch
472 in the width direction, each related to growth-applied pressure Δp by

473

474
$$\Delta L = a_L \Delta p \quad (1)$$

475
$$\Delta W = a_W \Delta p. \quad (2)$$

476

477 The “stretch coefficients” in length, a_L , and width, a_W , measure the stiffness of the cuticle (S5 File, Eq.
478 S14-S23). Smaller values correspond to a stiffer material, which is less able to stretch in response to pressure.
479 The stretch coefficients are constant in the linearly elastic regime and are determined by geometric constants
480 and material properties. The ratio of the change in length (Eq. 1) and width (Eq. 2) produces an experimentally
481 verifiable, pressure-independent relationship that depends only on the ratio of the geometric and material
482 properties. Eq. 9 predicts that during the linearly elastic regime, the ratio of growth in width to growth in length
483 is constant throughout a larval stage where the cuticle properties are fixed.

484

485
$$\frac{\Delta W}{\Delta L} = \frac{a_W}{a_L} = \text{constant} \quad (3)$$

486

487 In the non-linear stretch regime (Fig 5), growth continues to apply pressure to the cuticle uniformly in all
488 directions. As observed in *nek1-3(sv3)* mutants, the cuticle can become stiff when stretched beyond tolerance
489 [54]. Once outside of the linearly elastic regime, the cuticle hardly stretches, even under large forces. We
490 hypothesized that this shift from linear to nonlinear regimes provides a way for animals to sense their own size
491 and cues the larval-stage transition (Fig 5). In principle, this transition could occur in either the width or length
492 directions, or both, but our results are consistent with transitioning from linear to non-linear stretch in the length
493 direction and maintaining linear stretch in the width direction (Fig 6). In the nonlinear regime, the stretch in the
494 length direction in response to pressure becomes

495

496

$$\Delta L \approx \tilde{a}_L(p) \Delta p \quad (4)$$

497

498 The nonlinear “stretch coefficient,” $\tilde{a}_L(p)$, is no longer constant and decreases with increasing pressure. It is
499 smaller than a_L because the cuticle has become less elastic than in the linear regime. If the length-direction
500 enters the nonlinear regime and has reduced stretch response, while width has the same constant stretch
501 response then, we expect the $\frac{\Delta W}{\Delta L}$ ratio to increase

502

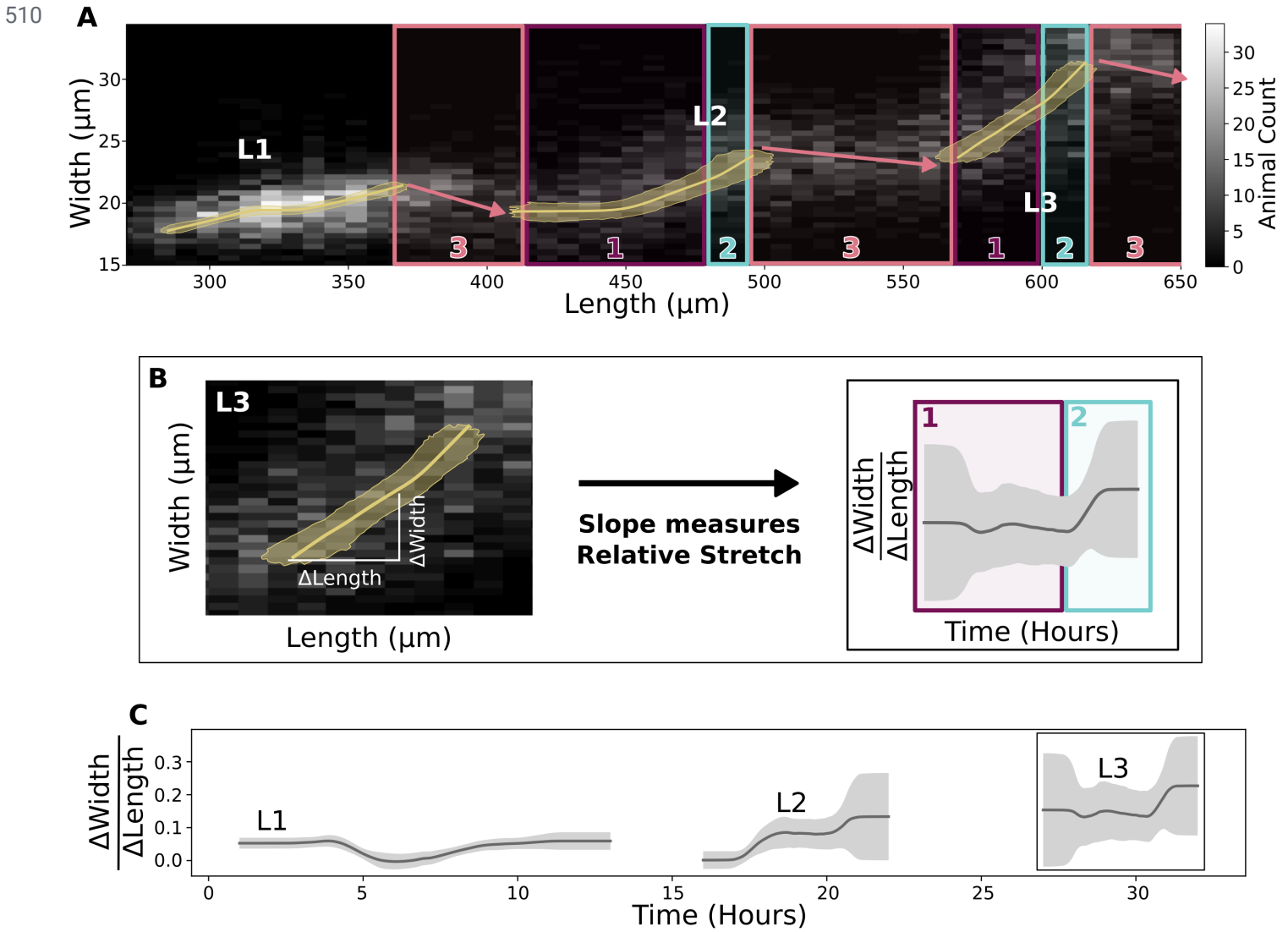
503

$$\frac{\Delta W}{\Delta L} |_{non-linear} = \frac{a_w}{\tilde{a}_L(p)} > \frac{a_w}{a_L} = \frac{\Delta W}{\Delta L} |_{linear} \quad (5)$$

504

505 During larval stage transition (Fig 5), a new, larger cuticle is formed beneath the old cuticle that is shed during
506 ecdysis. Because the old cuticle constrained growth in length, we predict a rapid increase in the length
507 direction when the constraint is removed. Nematode volume is conserved as growth does not occur during this
508 process. Therefore, the relaxation in length is accompanied by a corresponding decrease in width.

509



511 **Fig 6. Stretcher model analysis of replicate 2 COPAS BIOSORT data consistent with a length trigger for**
 512 **molting**

513 (A) A grayscale histogram of the width (y-axis) vs length (x-axis) of all sampled animals in replicate 2. The
 514 range of all bootstrap regressions is in gold. (B) The ratio of width to length stretch is the local slope. (C) Within
 515 a larval stage, the ratio of width to length stretch varies over time. The standard deviation captures population
 516 variation (grey) (S5 File, Eq. S26, S28).

517

518

519 To verify the shape dynamics predicted by the Stretcher model, we analyzed the relationship between
 520 nematode length and width over developmental time. All three regimes, linear stretch, non-linear stretch, and

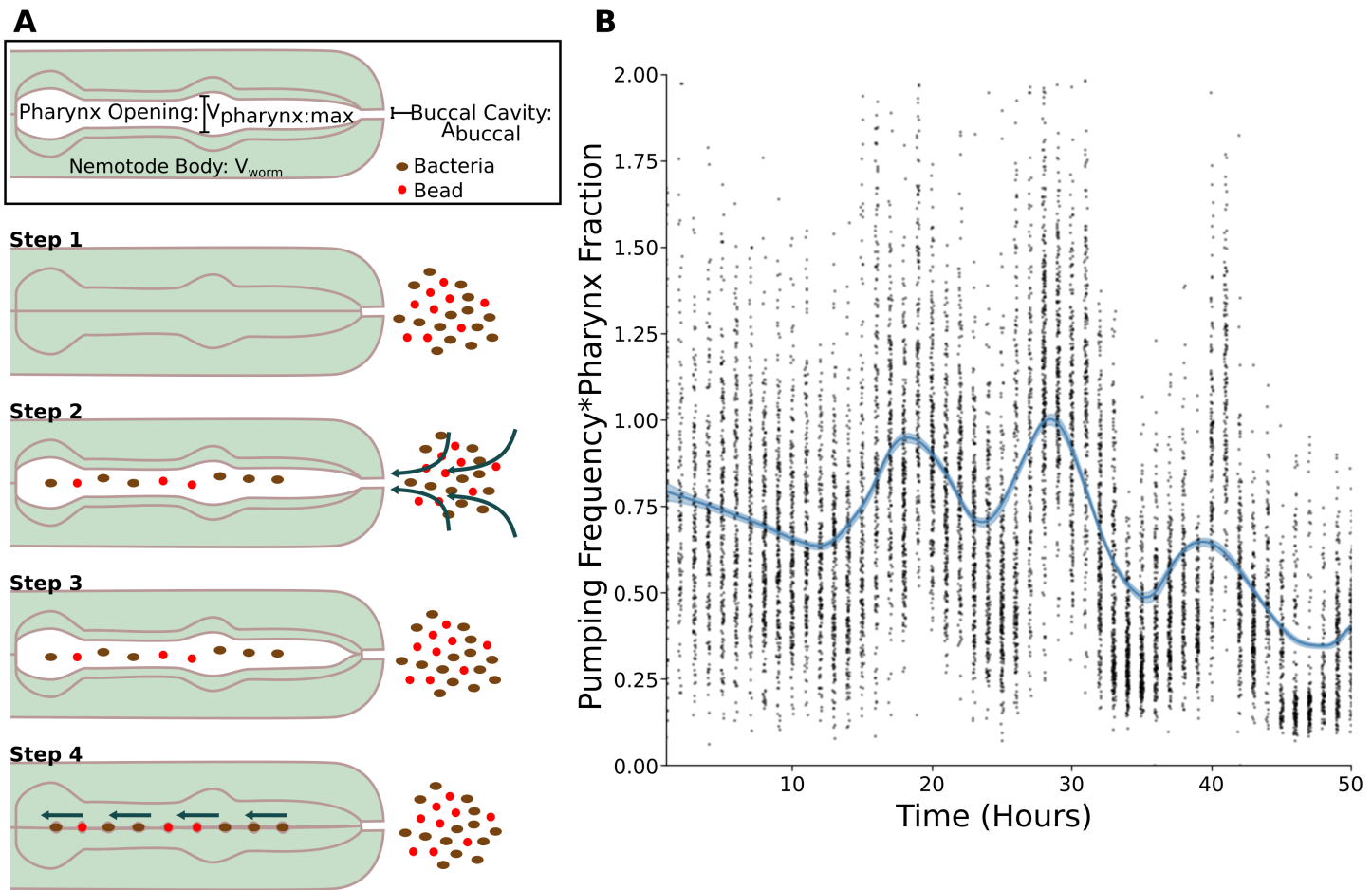
521 relaxation, predicted by the Stretcher model are detectable in the COPAS BIOSORT data (Fig 6). In all larval
522 stages, the instantaneous ratio $\frac{\Delta W}{\Delta L}$ was approximately constant for the majority of the time, consistent with a
523 linear stretch regime (Fig 6C). We observed a large slope decrease during the L1 stage, which could
524 correspond in time to the metabolic decision for entry into the dauer stage [59]. Near the end of L2 and L3
525 stages, we observed a sharp slope increase, supporting our predictions of a non-linear stretch regime in length
526 prior to lethargus. We note that the transitions between larval stages contain an increase in length and a
527 decrease in width (Fig 6A and S8 Fig) consistent with a length threshold in the Stretcher model. These results
528 suggest that the material properties of the cuticle, specifically the loss of ability to stretch in the length direction
529 in response to pressure from growth, generate a mechanical signal for the start of larval transition.

530

531 **Mechanical control of feeding and allocation of food constrain growth dynamics**

532 We have shown that changes in physical properties of the *C. elegans* cuticle precede the decision to initiate
533 molt and might serve as a cue for developmental timing. *C. elegans* must have mechanisms to control growth
534 throughout development, particularly in response to these cues. Like most species, *C. elegans*, do not increase
535 their growth rate indefinitely in response to increased food availability [27]. The animals could control growth
536 entirely through feeding rate, as they actively control the feeding rate [60] and stop feeding at the initiation of a
537 molt [22]. In addition to this mechanical control, they could use metabolic control to preemptively divert
538 ingested resources toward or away from growth. Metabolic processing of stored resources could be especially
539 useful if animals complete their molt and enter a food-limited environment. For these reasons, we investigated
540 the possible mechanical control of feeding (Fig 7A) and the metabolic control of the allocation of ingested food
541 toward organismal growth and development (Fig 8A). Using a quantitative feeding model, we calculated the
542 rate of mechanical feeding behavior from volume and food intake data. Additionally, we distinguish when
543 mechanical feeding rate or other regulatory mechanisms, such as metabolic control, are the primary drivers of
544 growth rate during *C. elegans* development.

545



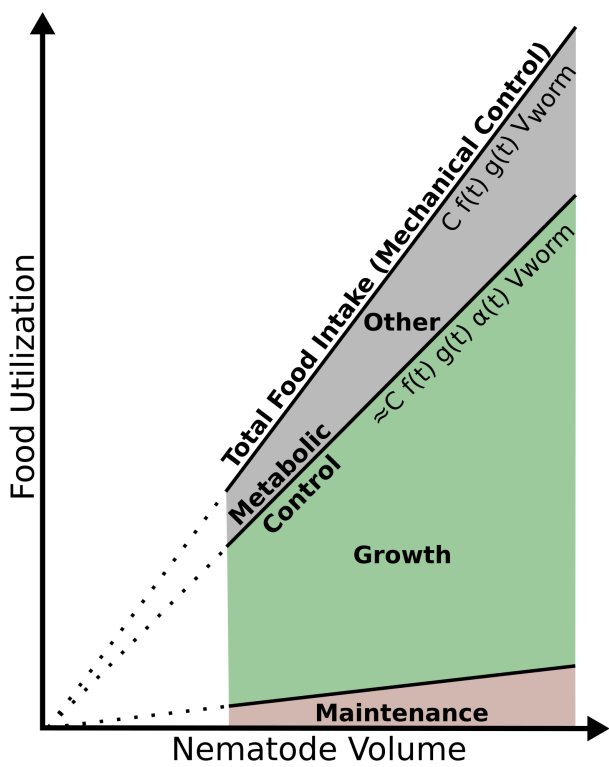
547 **Fig 7. Visualization and analysis of Feeding Model**

548 Schematics for food intake and utilization models are shown. (A) The buccal cavity is the opening through
549 which food enters. The pharynx is the cavity opened and closed by pharyngeal muscles that drives food intake.
550 (B) Product of pumping frequency and pharynx fraction, $f(t)g(t)$.

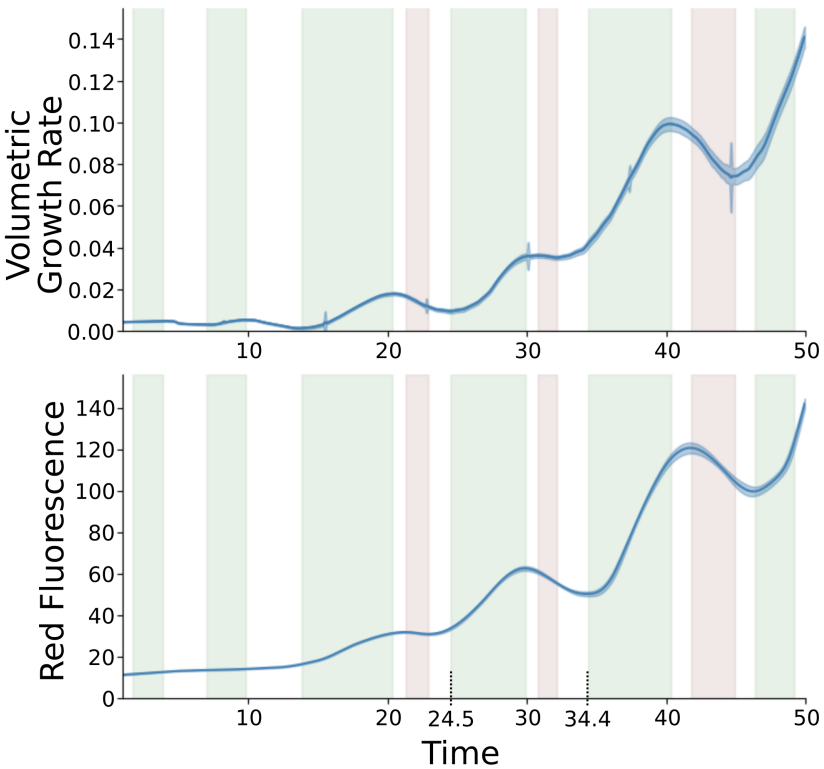
551

552

A



B



553 **Fig 8. Visualization and analysis of Food Utilization model.**

554 (A) The utilization of food resources as a function of animal volume. Total food intake controlled by feeding
555 rate. Maintenance is assumed to be negligible. Metabolic control partitions food resources used for growth
556 from other metabolic needs. (B) Dynamics of red fluorescence and volume growth rate. Errors on shaded
557 regions are ± 0.7 hours. These data are from replicate 2 and are representative of all replicates (S11 Fig).

558

559 Variation in pumping rate controls food uptake

560 *C. elegans* is a filter feeder that pumps its food through a cycle of pharyngeal muscle contractions and
561 relaxations that alternatively open and close the pharyngeal cavity. *C. elegans* are capable of actively
562 modulating the length of time used to contract or open a subset of the pharyngeal muscles [60]. Our feeding
563 model describes how control of this pumping period translates to changes in the rate of food uptake.

564

565 A single pumping cycle in which animals take up and transport food to the gut consists of four general steps
566 (Fig 7A). The cycle begins with relaxed pharyngeal muscles and a closed pharynx (step 1). The animal opens
567 the pharynx so that fluid and food flow through the buccal cavity and into the pharynx (step 2). The animal
568 cannot create a vacuum, so the volume of the cavity produced must be filled entirely by media and bacteria.
569 The animal relaxes the muscles that control the opening, stopping the flow of fluid through the buccal cavity
570 and trapping a volume of media approximately equal to the maximum volume of the pharynx (step 3). Finally,
571 the pharynx closes, extruding excess media and trapping bacteria and beads that are then 'swallowed' (step
572 4). The period of a single cycle varies throughout the life cycle of *C. elegans* [60].

573

574 We find a relationship between eating rate and animal volume. It has previously been suggested that the
575 cross-sectional area of the buccal cavity is a limiting factor in the rate of food intake [26]. However the volume
576 of the pharynx is filled each pumping period so the pharynx volume, not the cross-sectional area, sets food
577 uptake rate. We express pharynx volume as a fraction, $g(t)$, of nematode volume,
578 $V_{pharynx:max}(t) = g(t) \cdot V_{worm}(t)$. As the pumping period is much faster (roughly 200 ms in adults) [60] than the
579 rate of measured growth (hours), we averaged the food intake rate, $\frac{dV_{food}}{dt}$, over a single pumping period (S5
580 File, Eq. S1-S6) to obtain

581

582

$$\frac{dV_{food}}{dt} = Cf(t)g(t)V_{worm}. \quad (6)$$

583

584 Here $f(t)$ is the pumping frequency and the inverse of the period of a single pump. Both pumping frequency,
585 $f(t)$, and the fractional pharynx size, $g(t)$, vary over the animal's life cycle.

586

587 By using red fluorescence as a proxy measurement for food intake rate and calculated volume we estimated
588 the product of pumping rate and pharynx fraction, $f(t)g(t) \propto \frac{Red}{V_{worm}}$, over time. The product oscillated within a
589 larval stage and decreased across larval stages (Fig 7B). The minima of the product of pumping frequency and

590 pharynx fraction occurred during molt times, consistent with prior knowledge [22,25]. Pharynx length has been
591 shown to decrease over development [61] and a similar trend in pharynx volume could explain the slow
592 decrease in the product of pumping frequency and pharynx fraction.

593

594 **Changes in food utilization coincide with molts**

595 To understand whether the mechanical feeding process or metabolic regulation is the primary driver of growth
596 and development, we describe how food is utilized once it is ingested by *C. elegans*. We assumed three
597 general categories of food utilization: maintenance, growth, and all other processes. We assumed that, when
598 animals are not food restricted the maintenance resource requirement is negligible compared to the food
599 utilized for growth. The rate of food conversion can be described by:

600

601
$$\frac{dV_{\text{worm}}(t)}{dt} = \eta(t)\alpha(t)\frac{dV_{\text{food}}}{dt}(t) \quad (7)$$

602

603 Here, $\frac{dV_{\text{food}}}{dt}$ is the instantaneous rate of food intake (averaged over a single pump), $\eta(t)$ is the metabolic
604 efficiency of converting food to growth, and $\alpha(t)$ is the fraction of food used for growth as opposed to other
605 metabolic processes. If $\eta(t)$ and $\alpha(t)$ are constant then Eq. (4) predicts the rate of volumetric growth is directly
606 proportional to the rate of food consumption. If, instead, efficiency of food utilization or the fraction of food
607 utilized for growth are not constant, then volumetric growth rate is no longer proportional to food consumption
608 rate and metabolic or regulatory control must play a role in driving the growth rate.

609

610 Feeding rate (using red fluorescence as a proxy) and volume growth rate (numerically differentiated from the
611 volume regression) are highly correlated throughout much of *C. elegans* development (Fig 8B). Each larval
612 stage consists of three types of dynamics: steady growth during which food intake and growth rate are both
613 increasing (green), preparation for molt during which food intake and growth rate are both decreasing (red),
614 and transition regions where food intake and growth rate are uncorrelated (white). To illustrate how these
615 dynamics correspond to the progression within a larval stage, consider the L3 larvae in replicate 2. At hour

616 24.5, both growth rate and food intake rate increased corresponding to the start of the third larval stage for the
617 population average. Until hour 29.8, the population grew steadily, and food intake and growth rate both
618 increased (green). Between hour 29.8 and 30.8 (white), food intake decreased and growth rate increased,
619 marking a transition from the steady growth (green) to the molt preparation regime (red). Between hours 30.8
620 and 32.1, the animals prepared to initiate molts, and both the growth rate and food intake rate decreased (red).
621 Between hours 32.1 and 34.4 (white), the animals' growth rate increased once again while the food intake rate
622 continued to decrease corresponding to the end of the molt and start of the L4 larval stage. Similar dynamics
623 occurred in the L2 and L3 larval stages. The L1 larval stage followed different dynamics, likely due to the dauer
624 decision.

625

626 During steady growth (green) and molt initiation (red), it is likely that growth is controlled by the rate of food
627 intake and thus under mechanical control by the animal. Loss of correlation between growth rate and food
628 intake rate (white) implies food intake rate can no longer be the primary driver of changes in growth rate. Either
629 the efficiency of metabolism, captured by $\eta(t)$, or the resource allocation toward growth, captured by $\alpha(t)$,
630 must vary at these times. In either case, the lack of correlation before and after each molt suggests other
631 regulatory mechanisms must be at play during these times.

632

633 Feeding rate and volumetric growth rate share a complex relationship with *C. elegans* development; food
634 intake and growth rate are highly correlated, except at larval stage transitions and possible key developmental
635 transitions. Notably, the metabolic decision indicated by the transition from increasing to decreasing growth
636 and food intake rates (Fig 8B) occurred at approximately the same times as the increase in slope predicted as
637 a cue for molt initiation by the Stretcher model (Fig 6). This correlation suggests that the cuticle reaches its
638 maximum stretch in length and a metabolic decision to reallocate food resources growth occurs at the same
639 time. This result supports the hypothesis that a physical threshold in stretch triggers metabolic decisions to
640 enter a molt (S10 Fig).

641

642 Discussion

643 Using an integrated image-based and flow-based phenotyping strategy to precisely evaluate feeding, growth,
644 and molt dynamics at high replication, we detected oscillations in feeding behavior consistent with larval
645 progressions and used these dynamics to define larval stages. We observed changes in body shape at each
646 larval-stage transition that are consistent with differences in physical cuticle properties along length or width
647 (anisotropy). These results suggest that animals sense their size and control molt timing by detecting the
648 physical stretch of the cuticle. To understand whether *C elegans* control growth through moderating the
649 physical uptake of nutrients or through metabolic regulation of the allocation of consumed resources we
650 applied mathematical models of feeding-limited growth to our data. We predicted that volumetric growth rate
651 was primarily controlled by *C. elegans* feeding rate for most of development, yet at molts and during a period of
652 the L1 larval stage, other regulatory processes drive growth. These results demonstrate two mechanisms by
653 which physical constraints can influence developmental timing and growth rate.

654

655 Cuticle stretch controls the timing of larval-stage transitions

656 Measurement of both animal length and width allowed us to observe changes in body shape as well as body
657 size. We propose that a “Stretch threshold” along the body length axis acts as a trigger to larval-stage
658 transitions. For cuticle stretch to trigger larval-stage transitions, animals must either have the ability to measure
659 the amount the cuticle has stretched or the stiffness of the cuticle. Across biological systems, cells can respond
660 to the stiffness of their environment using mechanosensitive components [62,63], but few examples in tissues
661 or whole-organisms are known. In *C. elegans*, it has been demonstrated that hemidesmosomes, which
662 connect the cuticle and the epidermis, are mechanosensitive during embryogenesis [64,65]. Additionally,
663 dense bodies, which connect the epidermis and muscles, are hypothesized to be mechanosensitive as well
664 ([24,66–68]. Changes in cuticle composition, and presumably stiffness, have been shown to also affect well
665 known growth controlling pathways such as the BMP signaling pathway [69]. These possible mechanosensitive
666 components could monitor the stiffness of the cuticle and be part of the signaling pathways that regulate

667 larval-stage transitions. Further experiments are required to explicitly test whether these components control
668 larval-stage transitions.

669

670 Our analysis of width-to-length ratio variation over larval stages provides a first approximation of the timing of
671 larval-stage transition cues and cuticle stretch properties (Fig 8). The sudden increase we observed in the
672 width-to-length ratio suggests a length stretch threshold. Single-worm, high frequency measurements targeting
673 hours surrounding the sudden width-to-length ratio increase, are needed to better resolve cuticle shape
674 dynamics. Higher time resolution would also minimize edge effects (S12 Fig), which likely caused the
675 unpredicted width-to-length ratio increase observed at the start of larval stage L2 (Fig 8C). Measurements of
676 animal length and width provide a total stiffness estimate but do not allow us to distinguish the contributions of
677 cuticle stiffness from other tissues. To investigate cuticle properties, independent of other nematode tissues
678 and organs, experiments must probe the stiffness of free cuticles.

679

680 **Physical constraints on feeding influence growth dynamics**

681 Our mechanical feeding model defines a relationship between food availability, food intake rate, food utilization,
682 and growth rate. We distinguished between food intake rate and pumping rates by modeling the physical
683 process of feeding. The results of our analysis are consistent with both an oscillation in pumping rates [22] and
684 a slow change in pharynx size throughout development [61]. Previous research suggested that pumping
685 frequencies within a larval stage are constant with sudden transitions between lethargus and pumping [51].
686 However, we were unable to resolve sudden transitions because of the continuous smoothing of the kernel
687 regression method used and population effects (Fig 7B). Previous work has shown that growth rate increases
688 with increasing food availability up to a saturation limit [27]. Varying bacterial concentration levels in future
689 experiments would allow us to distinguish whether mechanical control of food intake or metabolic control of
690 food utilization determine the upper bound on growth rate.

691

692 Our analysis of the relationship between growth rate and food intake rate demonstrated short periods of time
693 during which growth rate and food intake rate were not correlated. These periods may be developmental points
694 in which metabolic decisions are being made and food and energy resource allocation is changing. Within the
695 L2 and L3 stages we observed a loss of correlation between growth rate and food intake twice. The first of
696 these time periods corresponds to the times at which the width-to-length ratio drastically changes and the
697 second corresponds to ecdysis (S10 Fig). The loss of correlation between growth and food intake motivates
698 the need for further metabolomic experiments to probe metabolic regulation surrounding larval stage
699 transitions.

700

701 In the analysis of both the Stretcher and feeding models, we found that the L1 larval stage has different
702 dynamics than other larval stages. We observed a decrease in growth rate with no associated decrease in
703 feeding rate, corresponding to a mid-stage resource reallocation, that does not occur in any other larval stage,
704 possibly showing the dauer decision [59]. Additionally, within the L1 stage, the relative stretch measured in
705 width and length did not follow the pattern observed in other larval stages. We observed a mid-stage dip in the
706 width-to-length ratio that is otherwise approximately constant throughout the L1 stage. As animals reallocate
707 food resources around the dauer decision, they also undergo a change in shape suggesting either directed
708 growth or structural changes to either the cuticle or animal body during L1 (Fig 3, Fig 6, S8 Fig). Future
709 experiments exploring the structural properties of cuticles at all larval stages may help to determine where the
710 L1 shape changes originate.

711

712 Metazoan development comprises complex interactions of growth regulation across diverse scales

713 Our results demonstrate that *C. elegans* uses physical constraints on animal size and feeding rate to control
714 growth rate and determine developmental transitions. The control of whole-organism growth requires cells,
715 tissues, and organs to orchestrate final size and cell number. In *C. elegans*, cell number is precisely defined
716 and invariant from animal to animal [70], so the final adult size of an individual must come from cell size as
717 opposed to number. Future studies should focus on how whole-organism size is determined by the integration

718 of cell, tissue, and organ size. By incorporating these different developmental scales, the Stretcher model can
719 be refined to completely describe how physical constraints on parts of the organism impact the whole. *C.*
720 *elegans* gives investigators a method to investigate animal-to-animal variation in developmental trajectories
721 across each of these scales.

722

723 References

- 724 1. Hone DWE, Benton MJ. The evolution of large size: how does Cope's Rule work? *Trends Ecol Evol.*
725 2005;20: 4–6.
- 726 2. Björklund M. Cell size homeostasis: Metabolic control of growth and cell division. *Biochim Biophys Acta*
727 *Mol Cell Res.* 2019;1866: 409–417.
- 728 3. Willis L, Huang KC. Sizing up the bacterial cell cycle. *Nat Rev Microbiol.* 2017;15: 606–620.
- 729 4. Turner JJ, Ewald JC, Skotheim JM. Cell size control in yeast. *Curr Biol.* 2012;22: R350–9.
- 730 5. Donnan L, John PC. Cell cycle control by timer and sizer in Chlamydomonas. *Nature.* 1983;304: 630–633.
- 731 6. Wang P, Hayden S, Masui Y. Transition of the blastomere cell cycle from cell size-independent to
732 size-dependent control at the midblastula stage in *Xenopus laevis*. *J Exp Zool.* 2000;287: 128–144.
- 733 7. Tzur A, Kafri R, LeBleu VS, Lahav G, Kirschner MW. Cell growth and size homeostasis in proliferating
734 animal cells. *Science.* 2009;325: 167–171.
- 735 8. Pavelescu I, Vilarrasa-Blasi J, Planas-Riverola A, González-García M-P, Caño-Delgado AI, Ibañes M. A
736 Sizer model for cell differentiation in *Arabidopsis thaliana* root growth. *Mol Syst Biol.* 2018;14: e7687.
- 737 9. Sveiczer A, Novak B, Mitchison JM. The size control of fission yeast revisited. *J Cell Sci.* 1996;109 (Pt
738 12): 2947–2957.
- 739 10. Campos M, Surovtsev IV, Kato S, Paintdakhi A, Beltran B, Ebmeier SE, et al. A constant size extension
740 drives bacterial cell size homeostasis. *Cell.* 2014;159: 1433–1446.
- 741 11. Taheri-Araghi S, Bradde S, Sauls JT, Hill NS, Levin PA, Paulsson J, et al. Cell-size control and
742 homeostasis in bacteria. *Curr Biol.* 2015;25: 385–391.
- 743 12. Soifer I, Robert L, Amir A. Single-Cell Analysis of Growth in Budding Yeast and Bacteria Reveals a

- 744 Common Size Regulation Strategy. *Curr Biol.* 2016;26: 356–361.
- 745 13. Osella M, Nugent E, Cosentino Lagomarsino M. Concerted control of *Escherichia coli* cell division. *Proc
746 Natl Acad Sci U S A.* 2014;111: 3431–3435.
- 747 14. Jorgensen P, Tyers M. How cells coordinate growth and division. *Curr Biol.* 2004;14: R1014–27.
- 748 15. Wang P, Robert L, Pelletier J, Dang WL, Taddei F, Wright A, et al. Robust growth of *Escherichia coli*. *Curr
749 Biol.* 2010;20: 1099–1103.
- 750 16. Cadart C, Monnier S, Grilli J, Sáez PJ, Srivastava N, Attia R, et al. Size control in mammalian cells
751 involves modulation of both growth rate and cell cycle duration. *Nat Commun.* 2018;9: 3275.
- 752 17. Moss-Taylor L, Upadhyay A, Pan X, Kim M-J, O'Connor MB. Body Size and Tissue-Scaling Is Regulated
753 by Motoneuron-Derived Activin β in *Drosophila melanogaster*. *Genetics.* 2019;213: 1447–1464.
- 754 18. Spence AJ. Scaling in biology. *Curr Biol.* 2009;19: R57–61.
- 755 19. Uppaluri S, Weber SC, Brangwynne CP. Hierarchical Size Scaling during Multicellular Growth and
756 Development. *Cell Rep.* 2016;17: 345–352.
- 757 20. Wood WB. The Nematode *Caenorhabditis Elegans*. Cold Spring Harbor Laboratory; 1988.
- 758 21. Page AP, Johnstone IL. The cuticle. *WormBook.* 2007; 1–15.
- 759 22. Singh RN, Sulston JE. Some Observations On Moulting in *Caenorhabditis Elegans*. *Nematologica.*
760 1978;24: 63–71.
- 761 23. Monsalve GC, Van Buskirk C, Frand AR. LIN-42/PERIOD controls cyclical and developmental progression
762 of *C. elegans* molts. *Curr Biol.* 2011;21: 2033–2045.
- 763 24. Zaidel-Bar R, Miller S, Kaminsky R, Broday L. Molting-specific downregulation of *C. elegans* body-wall
764 muscle attachment sites: the role of RNF-5 E3 ligase. *Biochem Biophys Res Commun.* 2010;395:

- 765 509–514.
- 766 25. Byerly L, Cassada RC, Russell RL. The life cycle of the nematode *Caenorhabditis elegans*. I. Wild-type
767 growth and reproduction. *Dev Biol*. 1976;51: 23–33.
- 768 26. Knight CG, Patel MN, Azevedo RBR, Leroi AM. A novel mode of ecdysozoan growth in *Caenorhabditis*
769 *elegans*. *Evol Dev*. 2002;4: 16–27.
- 770 27. Uppaluri S, Brangwynne CP. A size threshold governs *Caenorhabditis elegans* developmental
771 progression. *Proc Biol Sci*. 2015;282: 20151283.
- 772 28. Tuck S. The control of cell growth and body size in *Caenorhabditis elegans*. *Exp Cell Res*. 2014;321:
773 71–76.
- 774 29. Patterson GI, Padgett RW. TGF beta-related pathways. Roles in *Caenorhabditis elegans* development.
775 *Trends Genet*. 2000;16: 27–33.
- 776 30. McKeown C, Praitis V, Austin J. *sma-1* encodes a betaH-spectrin homolog required for *Caenorhabditis*
777 *elegans* morphogenesis. *Development*. 1998;125: 2087–2098.
- 778 31. Madaan U, Yzeiraj E, Meade M, Clark JF, Rushlow CA, Savage-Dunn C. BMP Signaling Determines Body
779 Size via Transcriptional Regulation of Collagen Genes in *Caenorhabditis elegans*. *Genetics*. 2018;210:
780 1355–1367.
- 781 32. Page AP, Johnstone IL. The cuticle. *WormBook*; 2007.
- 782 33. Baugh LR. To grow or not to grow: nutritional control of development during *Caenorhabditis elegans* L1
783 arrest. *Genetics*. 2013;194: 539–555.
- 784 34. Hu PJ. Dauer. *WormBook*; 2018.
- 785 35. Mörck C, Pilon M. *C. elegans* feeding defective mutants have shorter body lengths and increased

- 786 autophagy. *BMC Dev Biol.* 2006;6: 39.
- 787 36. Cook DE, Zdraljevic S, Tanny RE, Seo B, Riccardi DD, Noble LM, et al. The Genetic Basis of Natural
788 Variation in *Caenorhabditis elegans* Telomere Length. *Genetics.* 2016;204: 371–383.
- 789 37. Andersen EC, Bloom JS, Gerke JP, Kruglyak L. A variant in the neuropeptide receptor npr-1 is a major
790 determinant of *Caenorhabditis elegans* growth and physiology. *PLoS Genet.* 2014;10: e1004156.
- 791 38. Stiernagle T. Maintenance of *C. elegans*. *WormBook*; 2006.
- 792 39. Abràmoff MD, Magalhães PJ, Ram SJ. Image processing with ImageJ. *Biophotonics international.*
793 2004;11: 36–42.
- 794 40. Andersen EC, Shimko TC, Crissman JR, Ghosh R, Bloom JS, Seidel HS, et al. A Powerful New
795 Quantitative Genetics Platform, Combining *Caenorhabditis elegans* High-Throughput Fitness Assays with
796 a Large Collection of Recombinant Strains. *G3* . 2015;5: 911–920.
- 797 41. Shimko TC, Andersen EC. COPASutils: An R Package for Reading, Processing, and Visualizing Data from
798 COPAS Large-Particle Flow Cytometers. *PLoS ONE.* 2014. p. e111090. doi:10.1371/journal.pone.0111090
- 799 42. Scrucca L, Fop M, Murphy TB, Raftery AE. mclust 5: Clustering, Classification and Density Estimation
800 Using Gaussian Finite Mixture Models. *R J.* 2016;8: 289–317.
- 801 43. Smith MV, Boyd WA, Kissling GE, Rice JR, Snyder DW, Portier CJ, et al. A discrete time model for the
802 analysis of medium-throughput *C. elegans* growth data. *PLoS One.* 2009;4: e7018.
- 803 44. Hermann E. lokern: Kernel Regression Smoothing with Local or Global Plug-in Bandwidth. R package
804 version 1.1-8. 2016. Available: <https://CRAN.R-project.org/package=lokern>
- 805 45. Sakamoto Y, Ishiguro M, Kitagawa G. Akaike information criterion statistics. Dordrecht, The Netherlands:
806 D Reidel. 1986;81: 26853.

- 807 46. Schwarz G. Estimating the Dimension of a Model. *aos*. 1978;6: 461–464.
- 808 47. Kass RE, Raftery AE. Bayes Factors. *J Am Stat Assoc*. 1995;90: 773.
- 809 48. Burnham KP, Anderson DR. *Model Selection and Multimodel Inference: A Practical Information-Theoretic*
810 Approach. Springer Science & Business Media; 2007.
- 811 49. Lokern: Kernel regression smoothing with local or global plug-in bandwidth. [cited 16 Mar 2021]. Available:
812 <https://CRAN.R-project.org/package=lokern>
- 813 50. Cassada RC, Russell RL. The dauerlarva, a post-embryonic developmental variant of the nematode
814 *Caenorhabditis elegans*. *Dev Biol*. 1975;46: 326–342.
- 815 51. Nika L, Gibson T, Konkus R, Karp X. Fluorescent Beads Are a Versatile Tool for Staging *Caenorhabditis*
816 *elegans* in Different Life Histories. *G3* . 2016;6: 1923–1933.
- 817 52. Vuaridel-Thurre G, Vuaridel AR, Dhar N, McKinney JD. Computational Analysis of the Mutual Constraints
818 between Single-Cell Growth and Division Control Models. *Adv Biosyst*. 2020;4: e1900103.
- 819 53. Brenner S. The genetics of *Caenorhabditis elegans*. *Genetics*. 1974;77: 71–94.
- 820 54. Yochem J, Lažetić V, Bell L, Chen L, Fay D. *C. elegans* NIMA-related kinases NEKL-2 and NEKL-3 are
821 required for the completion of molting. *Dev Biol*. 2015;398: 255–266.
- 822 55. Petzold BC, Park S-J, Ponce P, Roozeboom C, Powell C, Goodman MB, et al. *Caenorhabditis elegans*
823 body mechanics are regulated by body wall muscle tone. *Biophys J*. 2011;100: 1977–1985.
- 824 56. Cox GN, Staprans S, Edgar RS. The cuticle of *Caenorhabditis elegans*. II. Stage-specific changes in
825 ultrastructure and protein composition during postembryonic development. *Dev Biol*. 1981;86: 456–470.
- 826 57. Park S-J, Goodman MB, Pruitt BL. Analysis of nematode mechanics by piezoresistive displacement
827 clamp. *Proc Natl Acad Sci U S A*. 2007;104: 17376–17381.

- 828 58. Gilpin W, Uppaluri S, Brangwynne CP. Worms under Pressure: Bulk Mechanical Properties of *C. elegans*
829 Are Independent of the Cuticle. *Biophysical Journal*. 2015. pp. 1887–1898. doi:10.1016/j.bpj.2015.03.020
- 830 59. Golden JW, Riddle DL. The *Caenorhabditis elegans* dauer larva: developmental effects of pheromone,
831 food, and temperature. *Dev Biol*. 1984;102: 368–378.
- 832 60. Fang-Yen C, Avery L, Samuel ADT. Two size-selective mechanisms specifically trap bacteria-sized food
833 particles in *Caenorhabditis elegans*. *Proc Natl Acad Sci U S A*. 2009;106: 20093–20096.
- 834 61. Avery L. Food transport in the *C. elegans* pharynx. *Journal of Experimental Biology*. 2003. pp. 2441–2457.
835 doi:10.1242/jeb.00433
- 836 62. Schiller HB, Fässler R. Mechanosensitivity and compositional dynamics of cell-matrix adhesions. *EMBO*
837 *Rep*. 2013;14: 509–519.
- 838 63. Wolfenson H, Bershadsky A, Henis YI, Geiger B. Actomyosin-generated tension controls the molecular
839 kinetics of focal adhesions. *J Cell Sci*. 2011;124: 1425–1432.
- 840 64. Suman SK, Daday C, Ferraro T, Vuong-Breder T, Tak S, Quintin S, et al. The plakin domain of
841 VAB-10/plectin acts as a hub in a mechanotransduction pathway to promote morphogenesis.
842 *Development*. 2019;146. doi:10.1242/dev.183780
- 843 65. Zhang H, Landmann F, Zahreddine H, Rodriguez D, Koch M, Labouesse M. A tension-induced
844 mechanotransduction pathway promotes epithelial morphogenesis. *Nature*. 2011;471: 99–103.
- 845 66. Moerman DG, Williams BD. Sarcomere assembly in *C. elegans* muscle. *WormBook*. 2006; 1–16.
- 846 67. Costa M, Draper BW, Priess JR. The role of actin filaments in patterning the *Caenorhabditis elegans*
847 cuticle. *Dev Biol*. 1997;184: 373–384.
- 848 68. Broday L, Hauser CA, Kolotuev I, Ronai Z 'ev. Muscle-epidermis interactions affect exoskeleton patterning
849 in *Caenorhabditis elegans*. *Dev Dyn*. 2007;236: 3129–3136.

- 850 69. Madaan U, Faure L, Chowdhury A, Ahmed S, Ciccarelli EJ, Gumienny TL, et al. Feedback regulation of
851 BMP signaling by cuticle collagens. *Mol Biol Cell*. 2020;31: 825–832.
- 852 70. Horvitz HR, Sulston JE. Isolation and genetic characterization of cell-lineage mutants of the nematode
853 *Caenorhabditis elegans*. *Genetics*. 1980;96: 435–454.

854 Supporting Information Captions

855 **S1 Fig. Raw measurements of animal size.** Raw COPAS BIOSORT data of animal length (A), width (B), and
856 volume (C) are shown here. Smaller objects observed after 65 hours were the next generation of newly
857 hatched L1 larvae laid by the animals that developed during the time course.

858 **S2 Fig. Correlation analysis of body size measurements.** Manual measurements of animal length, width,
859 and estimated area were compared to COPAS BIOSORT measurements of TOF, norm.EXT, and EXT. Kendall
860 correlation value is shown in each plot.

861 **S3 Fig. Mixture modeling of COPAS BIOSORT data was used to prune data.** Mixture models of gaussian
862 distributions were fit to log transformed animal length (x-axis) and log transformed optical extinction (y-axis).
863 Data from each hour of the experiment was analyzed and processed to remove clusters that did not include
864 animal objects. All replicates were pruned independently; a subset of data from replicate 2 is shown here.
865 Panels indicate experimental hours from which data is taken.

866 **S4 Fig. Fluorescence measurements normalized by body size.** Red fluorescence beads were fed to
867 animals during experimentation and fluorescence data was collected by the COPAS BIOSORT. Fluctuations in
868 fluorescence indicate fluctuations in feeding behavior. Fluorescence data was normalized by body size
869 measurements to account for increases in body size. Dividing fluorescence by area was most successful in
870 normalizing fluorescence dynamics to account for changes in animal size over time.

871 **S5 Fig. Cuticles identified during periods of decreased feeding.** Images of wells collected during the
872 experiment were examined for evidence of shed cuticles. (A) Experimental hours where cuticles were identified
873 from images overlap with hours where population feeding behavior is low. Cuticles shed from the L4-Adult molt
874 persisted longer than previous larval stage cuticle debri. (B) Example image of animal without visible cuticle
875 during a period of elevated feeding. (C) Example image of an animal with visible cuticle indicating completion
876 of molt during a period of decreased feeding.

877 **S6 Fig. Volume growth data fit with linear, exponential, and cubic models.** Volume data of individuals in
878 time points defined as growth periods are analyzed for each stage. L1 stage was further separated into two
879 periods to account for the volume dip that occurs mid-stage.

880 **S7 Fig. Density plots of population size dynamics across all larval transitions.** Density curves of length
881 (A), width (B) and volume (C). Curves are divided into five quantiles and colored by the percentage of
882 quiescent animals present within that quantile. Molts are estimated to occur at experimental hours 14, 25, 36,
883 and 48 (see Methods).

884 **S8 Fig. Animals in all replicates, measured from images.** Animal length and width over *C. elegans*
885 development captured from image data. Higher noise levels in these measurements preclude accurate
886 regressions to individual larval stages. Length jumps and width dips are still apparent. Compare with Fig 6.

887 **S9 Fig. Comparison of red fluorescence regression and food intake rate with defecation calculation.**
888 Regression of red fluorescence (dashed pink) is compared to the intake rate of red beads accounting for
889 defecation rate (blue). Overlap of these two curves validates the use of red fluorescence as a proxy for food

890 **S10 Fig. Timeline of Food Utilization and Stretcher events.** In the first row (grey and white) we mark the
891 slopes determined in the Stretcher model. Transition from lighter to darker grey indicates a step increase in
892 slope corresponding to a stiffening cuticle in the length direction. White regions denote time between larval
893 stages. L2 and L3 are the only stages at which we have useful slope information due to the dauer decision in
894 L1 making transitions difficult to determine and the high level of population desynchronization in L4. In the
895 second row (green, red, and white) we mark the food and growth correlations found in (Fig 5B). Green
896 corresponds to times at which both growth rate and food rate are increasing. Red corresponds to times at
897 which both growth rate and food rate are decreasing. White corresponds to times at which growth rate and
898 food rate are uncorrelated. Transitions from green to red regions occur at roughly the same times as the
899 transition to a stiffer cuticle in the length direction.

900 **S11 Fig. Analysis of Food intake and growth rate correlation for all replicates.** Summary of analysis in
901 Fig. 8 for all replicates. Until larval stage L4, most replicates follow the same pattern of transitions from one
902 growth regime to the next. The time delay at transitions in later replicates can be explained by the temperature
903 gradient and differences in growth between replicates.

904 **S12 Fig. Stretcher model analysis of replicate 2 COPAS BIOSORT data for different stage thresholding.**
905 Compare to Fig 5. Larval hours defined by taking the ceiling of the lower boundary and the floor of the upper

906 boundary. This rounding method for larval stage definition demonstrates the sensitivity of the analysis to edge
907 effects. The unexpected step in the L2 larval stage (Fig 5) is significantly reduced with this rounding method.
908 **S13 Fig. Sensitivity analysis to moving average window size.** Varying lengths of window sizes (0.14 to
909 2.16 hours) were calculated for the *lokern* growth rate regression. Window size was increased until the growth
910 rate regression was smoothed. A window size of 1.44 hours (or 0.72 hours on either side of each time point)
911 was chosen to calculate the start and end times of each regime (Fig 8). Continued increase of window size
912 past 1.44 hours did not change the pattern of regimes or their boundaries significantly.

913

914 **S1 Table. Results of analysis of variance models fit to COPAS BIOSORT data.** Analysis of variance tests
915 were used to quantify the amount of variance in our data contributed by the sampling technique. The sampling
916 technique involved unbiased sampling of animals from six replicate populations and subsequent distribution
917 into multiple wells of a microtiter plate for analysis. We quantified the amount of variance contributed by
918 replicate and well. We find that the variance explained by well is nearly negligible whereas replicate contributes
919 minor variance in some measurements. Given this information, we deem the generated summary statistics an
920 appropriate representation of the population.

921 **S2 Table. Model fit criteria used to assess candidate growth models.** To determine the level of support for
922 each model, the candidate model with the smallest raw AIC/BIC was identified and compared to other AIC/BIC
923 values. If the delta value was greater than 6, the model with the smallest AIC/BIC value was denoted as the
924 best model. If the delta value was less than 6 but greater than 2, the model with the smallest AIC/BIC value
925 was determined to likely be the best model. If the delta value was less than 2, we are unable to distinguish the
926 model of best fit.

927

928 **S1 File. Incubator temperature data.** Temperature recordings of each position within the shaking incubator
929 used for growth experiment. (CSV)

930 **S2 File. COPAS BIOSORT growth data.** Raw growth data collected from the COPAS BIOSORT and
931 processed using the easysorter R package to compile information from each well. (CSV)

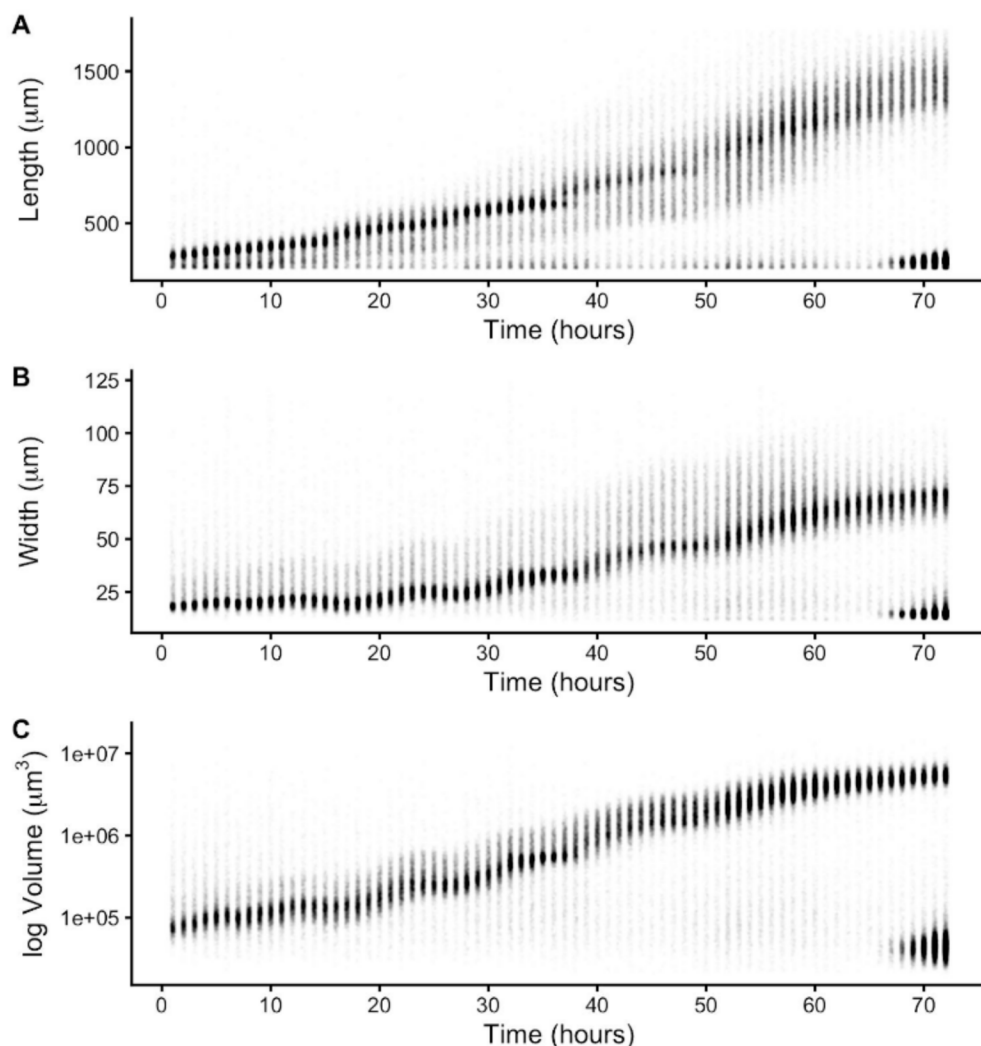
932 **S3 File. Pruned COPAS BIOSORT growth data.** Processed data from the COPAS BIOSORT following

933 implementation of the *mclust* R package and removal of clusters containing non-animal objects. (CSV)

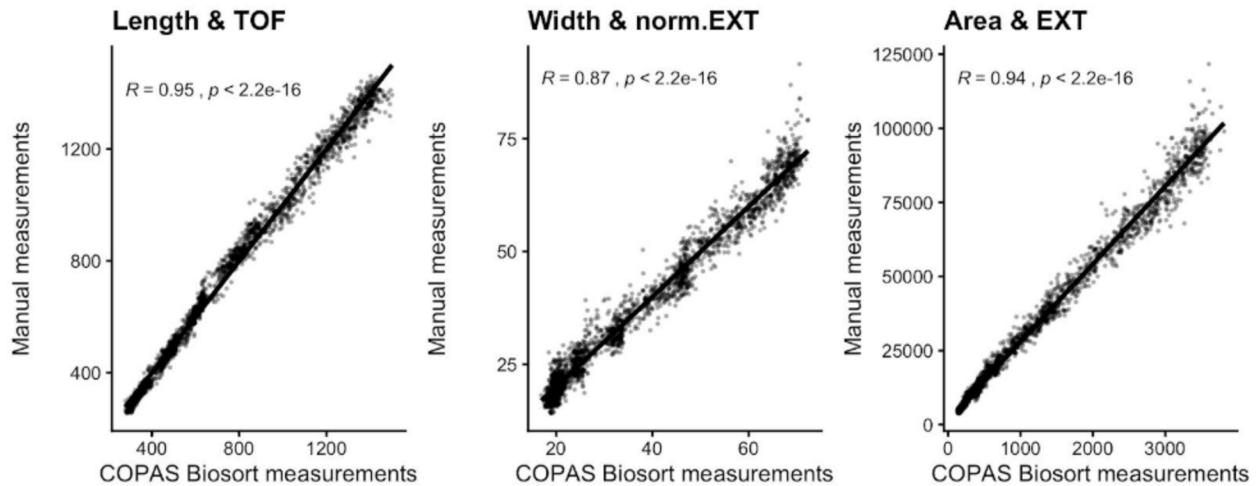
934 **S4 File. Image growth data.** Manual measurements of animal size acquired from images. (CSV)

935 **S5 File. Model derivations.**

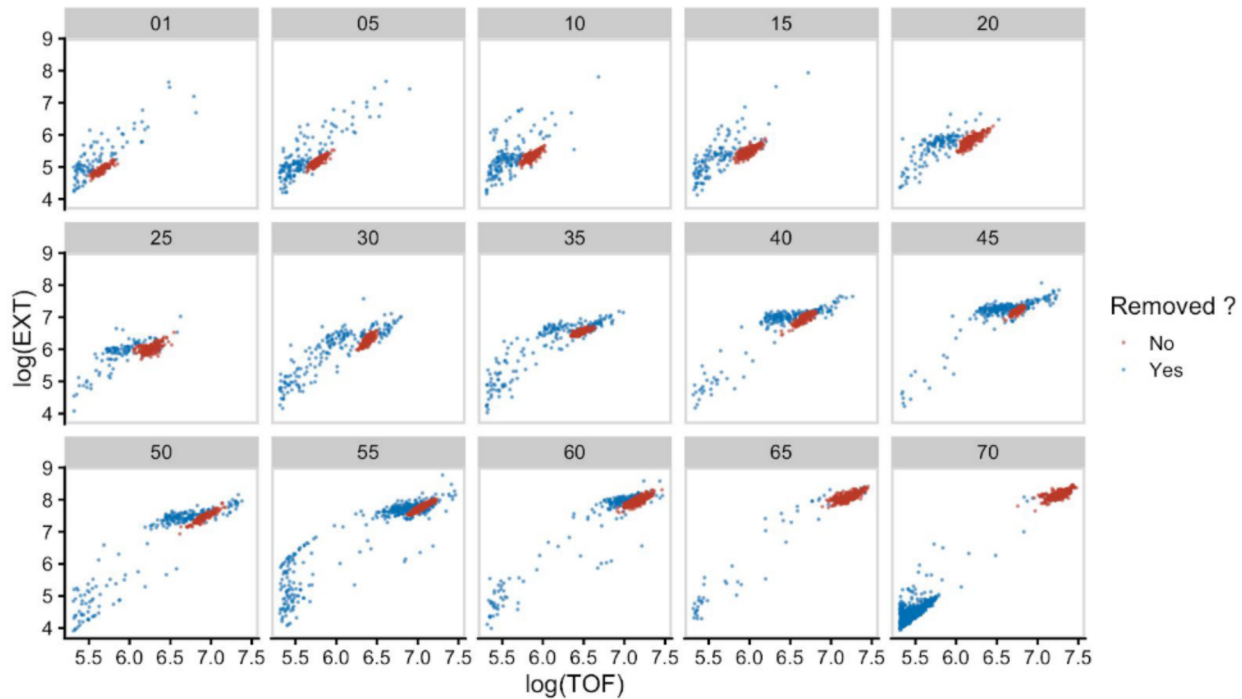
Supporting Information Figures



S1 Fig. Raw measurements of animal size. Raw COPAS BIOSORT data of animal length (A), width (B), and volume (C) are shown here. Smaller objects observed after 65 hours were the next generation of newly hatched L1 larvae laid by the animals that developed during the time course.



S2 Fig. Correlation analysis of body size measurements. Manual measurements of animal length, width, and estimated area were compared to COPAS BIOSORT measurements of TOF, norm.EXT, and EXT. Kendall correlation value is shown in each plot.



S3 Fig. Mixture modeling of COPAS BIOSORT data was used to prune data. Mixture models of gaussian distributions were fit to log transformed animal length (x-axis) and log transformed optical extinction (y-axis). Data from each hour of the experiment was analyzed and processed to remove clusters that did not include animal objects. All replicates were pruned independently; a subset of data from replicate 2 is shown here. Panels indicate experimental hours from which data is taken.

S1 Table. Results of analysis of variance models fit to COPAS BIOSORT data. Analysis of variance tests were used to quantify the amount of variance in our data contributed by the sampling technique. The sampling technique involved unbiased sampling of animals from six replicate populations and subsequent distribution into multiple wells of a microtiter plate for analysis. We quantified the amount of variance contributed by replicate and well. We find that the variance explained by well is nearly negligible whereas replicate contributes minor variance in some measurements. Given this information, we deem the generated summary statistics an appropriate representation of the population.

Response = Norm.Red

Terms	Df	Sum Sq	Mean Sq	F value	Pr(>F)	% Var Explained
hour	1	439.46	439.46	217762.01	0	54.34
replicate	6	165.82	27.64	13694.48	0	20.51
well	10	0.32	0.03	15.62	0	0.04
Residuals	100619	203.06	0	NA	NA	25.11

Response = Length

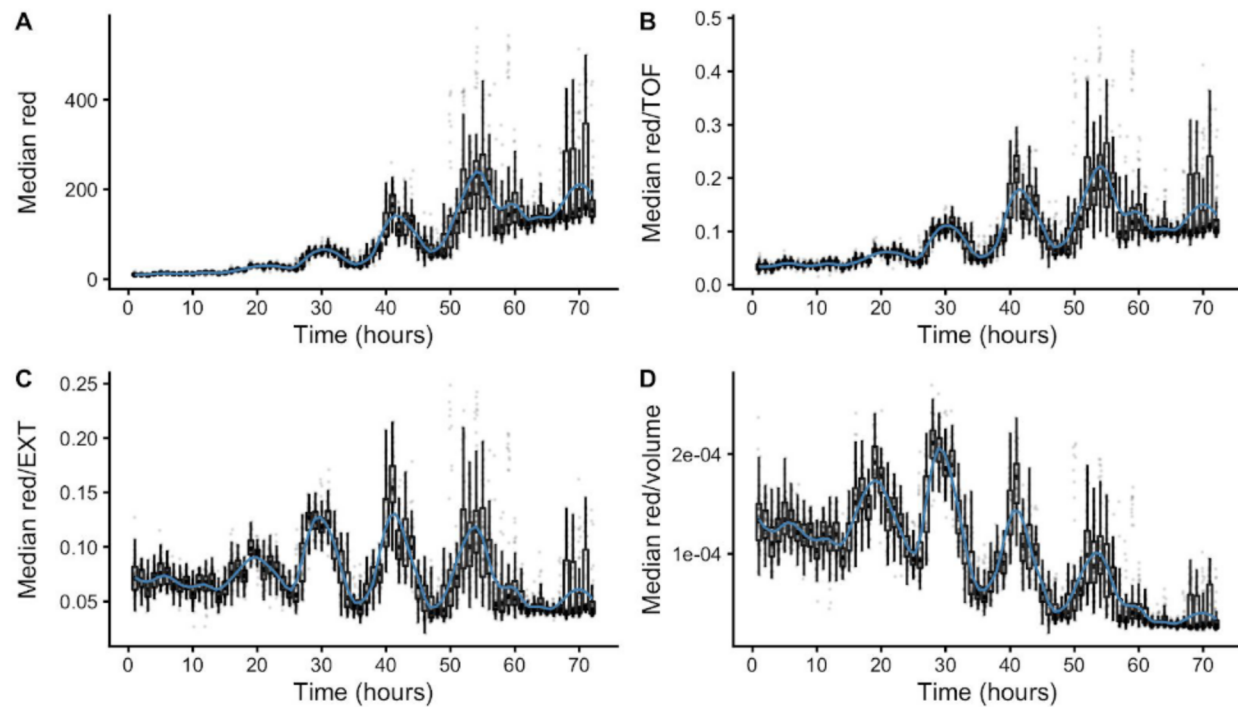
Terms	Df	Sum Sq	Mean Sq	F value	Pr(>F)	% Var Explained
hour	1	86190107879	86190107879	8223506	0	98.4
replicate	6	349438944	58239824	5557	0	0.4
well	10	834970	83497	8	0	0
Residuals	100619	1054582098	10481	NA	NA	1.2

Response = Width

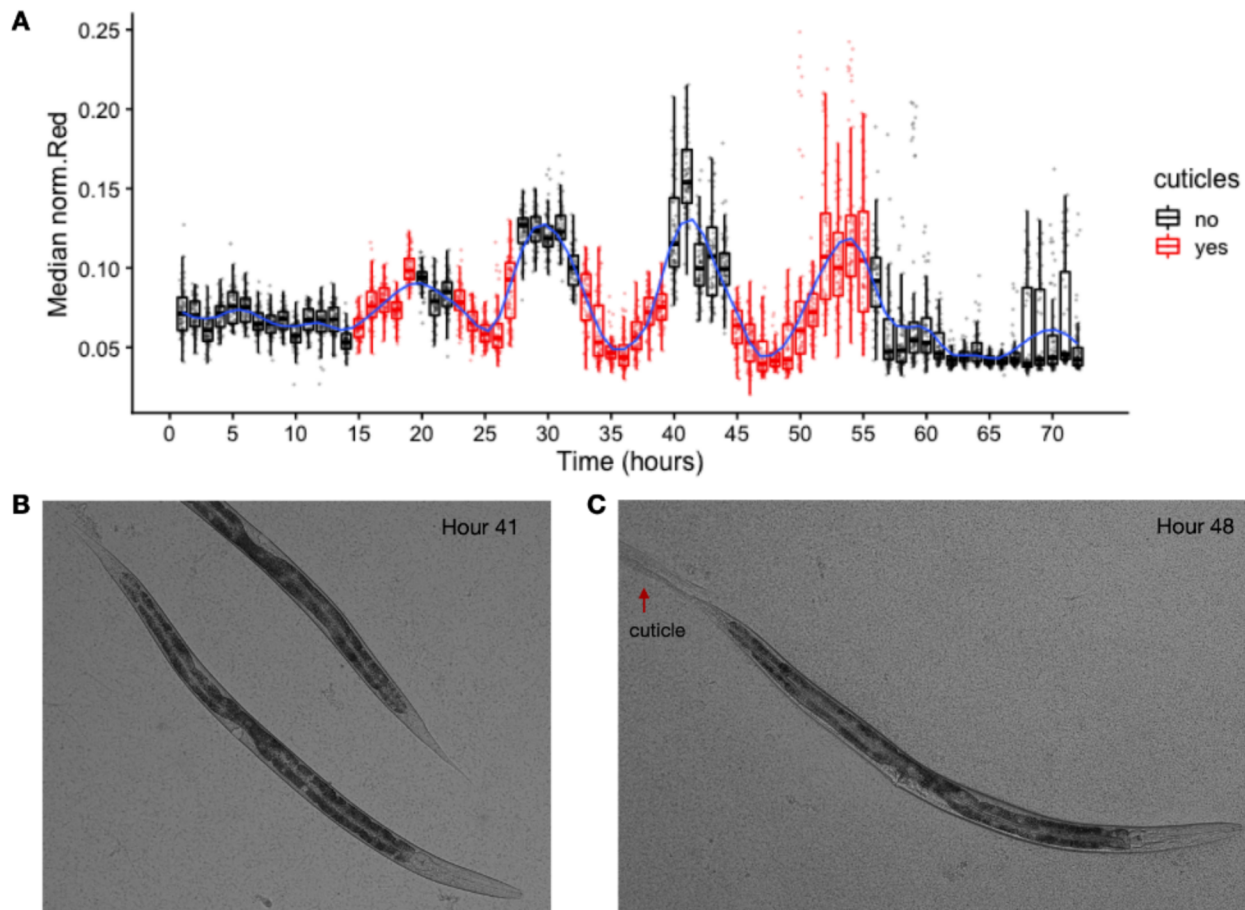
Terms	Df	Sum Sq	Mean Sq	F value	Pr(>F)	% Var Explained
hour	1	209090438.47	209090438.47	6950760.3	0	97.99
replicate	6	1266985.87	211164.31	7019.7	0	0.59
well	10	1495.32	149.53	4.97	0	0
Residuals	100619	3026786.99	30.08	NA	NA	1.42

Response = Volume

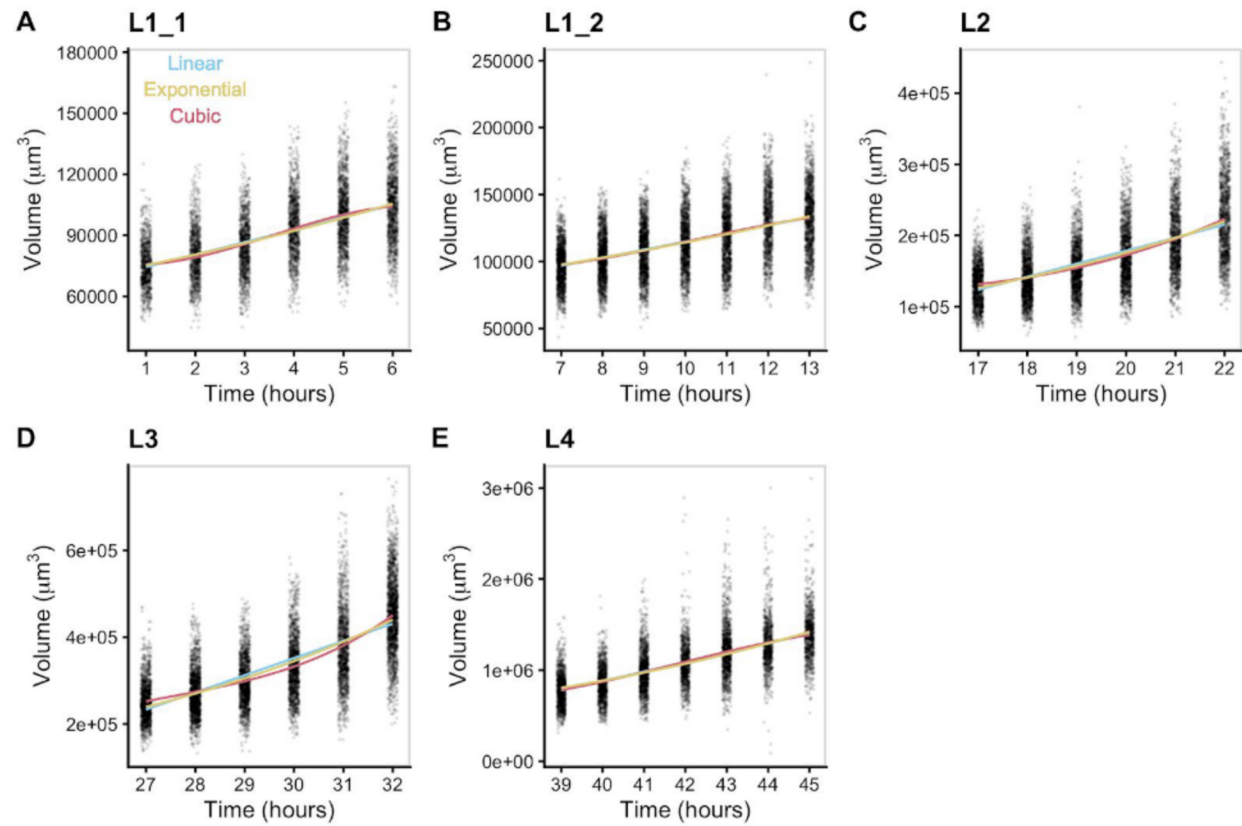
Terms	Df	Sum Sq	Mean Sq	F value	Pr(>F)	% Var Explained
hour	1	621712474191714688	621712474191714688	843342	0	84.08
replicate	6	43356968850687072	7226161475114512	9802	0	5.86
well	10	152458715405862	15245871540586	21	0	0.02
Residuals	100619	74176459811167296	737201321929	NA	NA	10.03



S4 Fig. Fluorescence measurements normalized by body size. Red fluorescence beads were fed to animals during experimentation and fluorescence data was collected by the COPAS BIOSORT. Fluctuations in fluorescence indicate fluctuations in feeding behavior. Fluorescence data was normalized by body size measurements to account for increases in body size. Dividing fluorescence by area was most successful in normalizing fluorescence dynamics to account for changes in animal size over time.



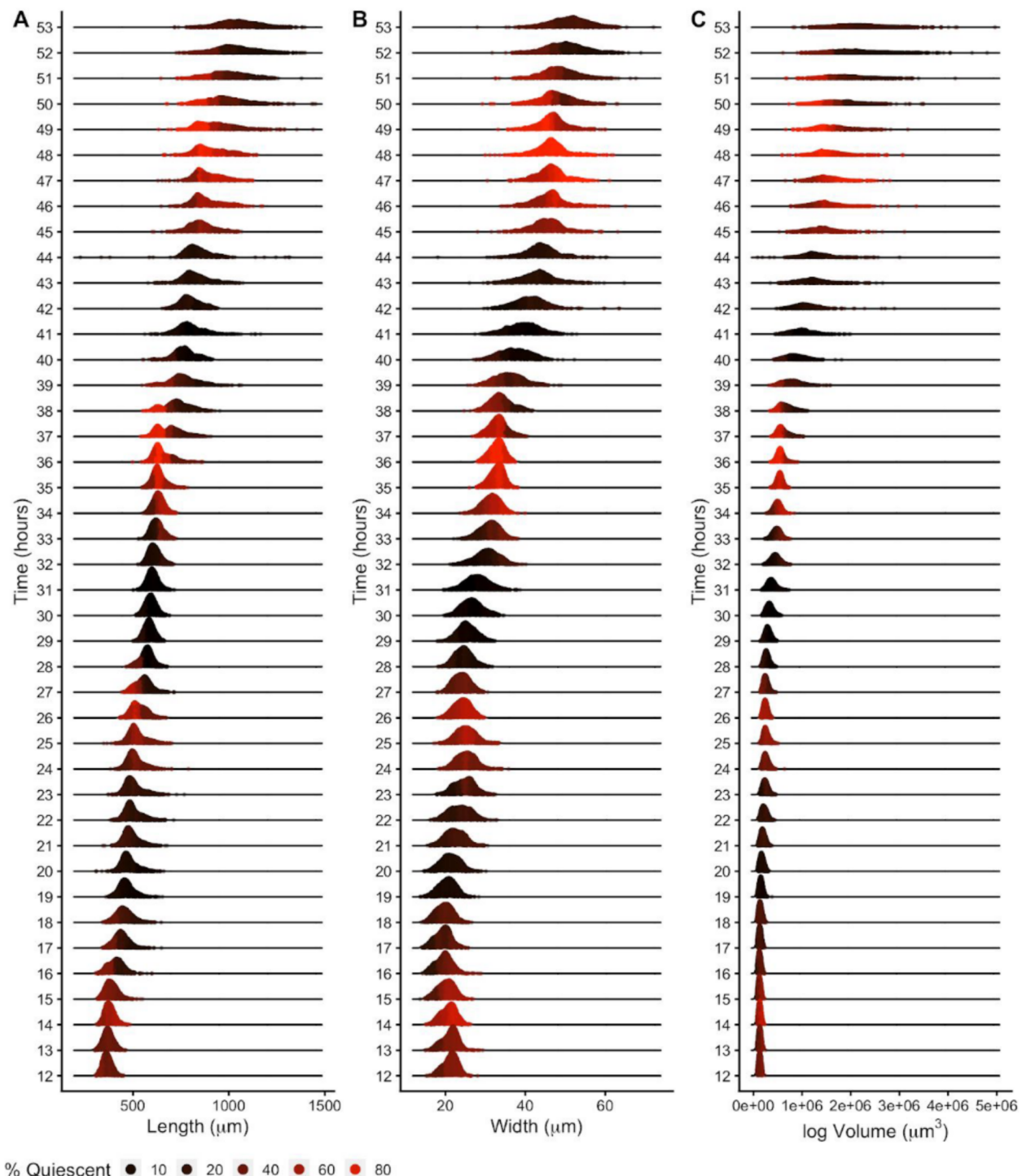
S5 Fig. Cuticles identified during periods of decreased feeding. Images of wells collected during the experiment were examined for evidence of shed cuticles. (A) Experimental hours where cuticles were identified from images overlap with hours where population feeding behavior is low. Cuticles shed from the L4-Adult molt persisted longer than previous larval stage cuticle debri. (B) Example image of animal without visible cuticle during a period of elevated feeding. (C) Example image of an animal with visible cuticle indicating completion of molt during a period of decreased feeding.



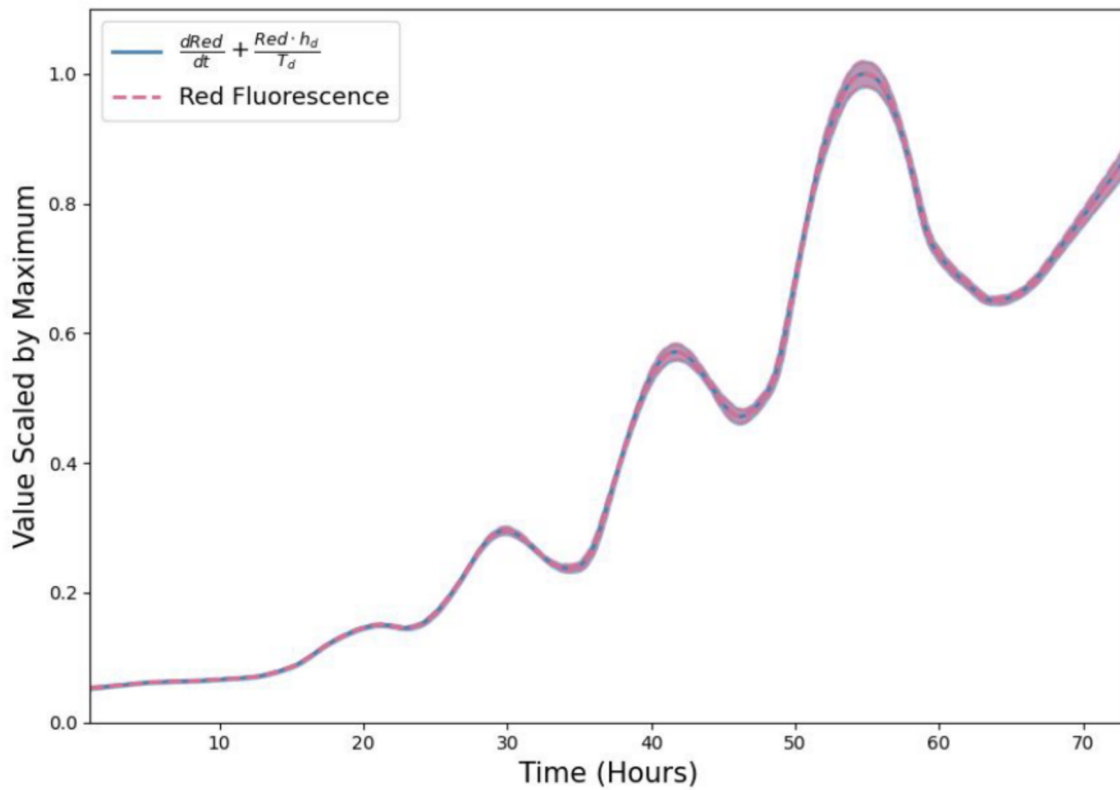
S6 Fig. Volume growth data fit with linear, exponential, and cubic models. Volume data of individuals in time points defined as growth periods are analyzed for each stage. L1 stage was further separated into two periods to account for the volume dip that occurs mid-stage.

S2 Table. Model fit criteria used to assess candidate growth models. To determine the level of support for each model, the candidate model with the smallest raw AIC/BIC was identified and compared to other AIC/BIC values. If the delta value was greater than 6, the model with the smallest AIC/BIC value was denoted as the best model. If the delta value was less than 6 but greater than 2, the model with the smallest AIC/BIC value was determined to likely be the best model. If the delta value was less than 2, we are unable to distinguish the model of best fit.

Stage	ΔAIC			ΔBIC				
	Linear	Exponential	Cubic	Linear	Exponential	Cubic	Best model by AIC	Best model by BIC
L1_1	17	21	0	4	9	0	Cubic	Likely Cubic
L1_2	2	4	0	0	2	12	Can't distinguish	Can't distinguish
L2	142	43	0	128	28	0	Cubic	Cubic
L3	374	145	0	360	131	0	Cubic	Cubic
L4	4	44	0	0	40	10	Likely Cubic	Linear

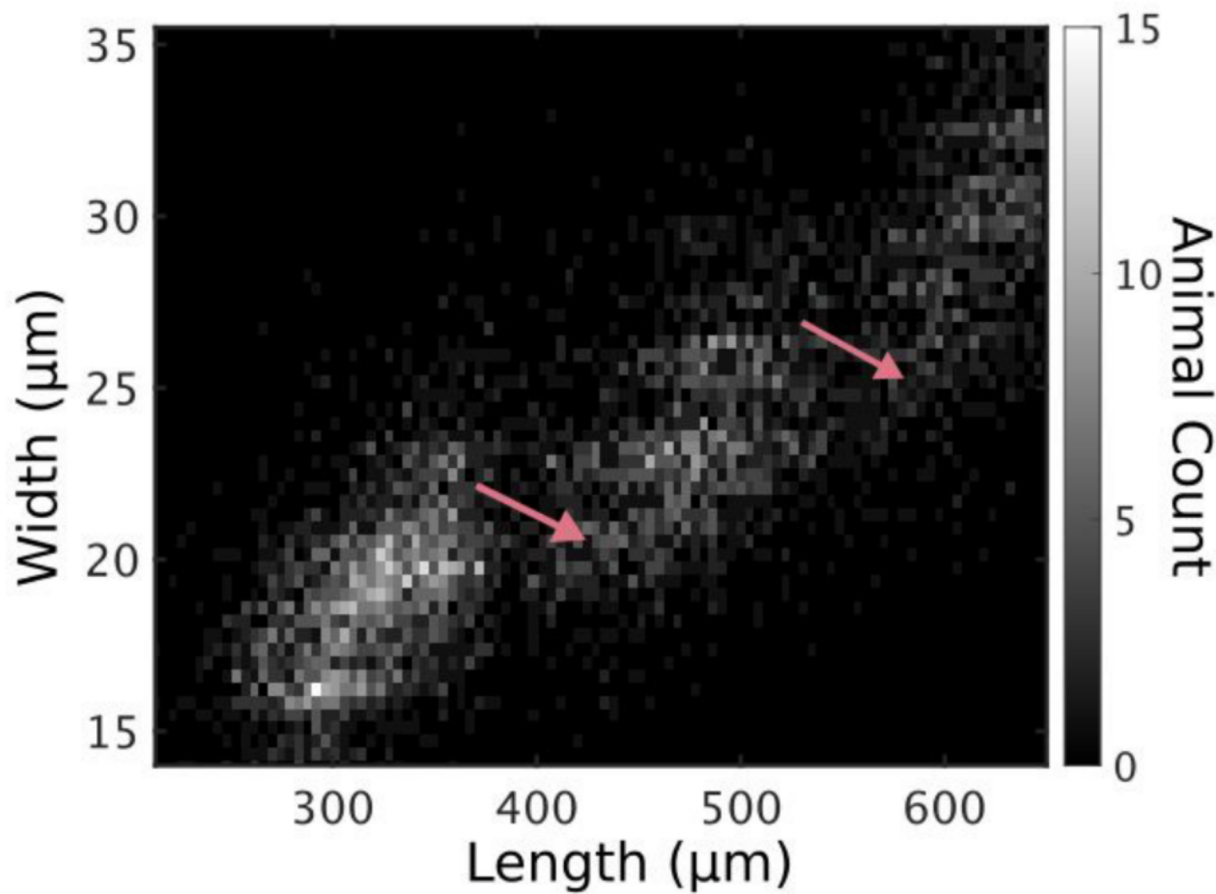


S7 Fig. Density plots of population size dynamics across all larval transitions. Density curves of length (A), width (B) and volume (C). Curves are divided into five quantiles and colored by the percentage of quiescent animals present within that quantile. Molts are estimated to occur at experimental hours 14, 25, 36, and 48 (see Methods).



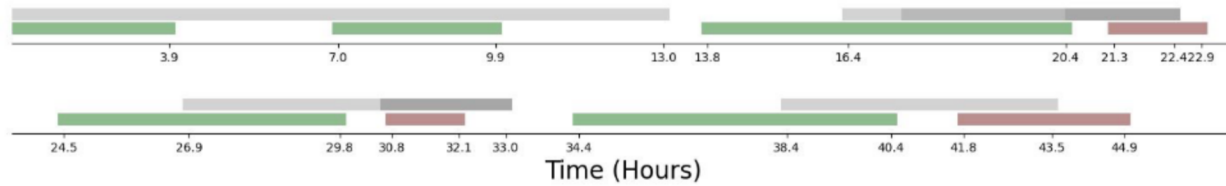
S9 Fig. Comparison of red fluorescence regression and food intake rate with defecation calculation

Regression of red fluorescence (dashed pink) is compared to the intake rate of red beads accounting for defecation rate (blue). Overlap of these two curves validates the use of red fluorescence as a proxy for food.



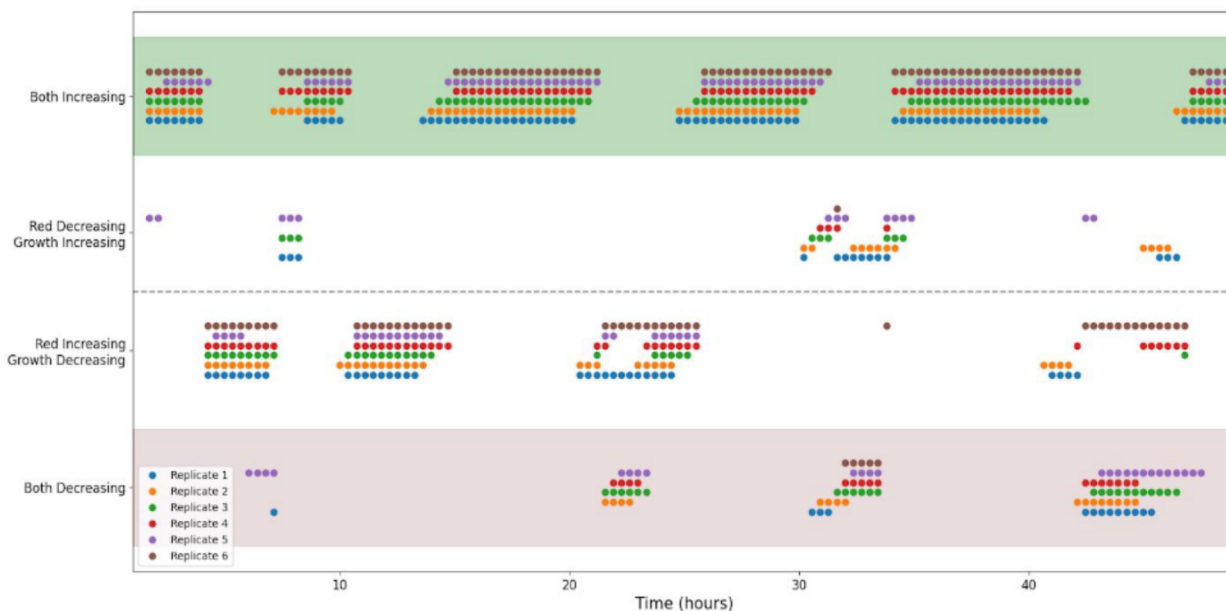
S8 Fig. Animals in all replicates, measured from images

Animal length and width over *C. elegans* development captured from image data. Higher noise levels in these measurements preclude accurate regressions to individual larval stages. Length jumps and width dips are still apparent. Compare with Fig 6.



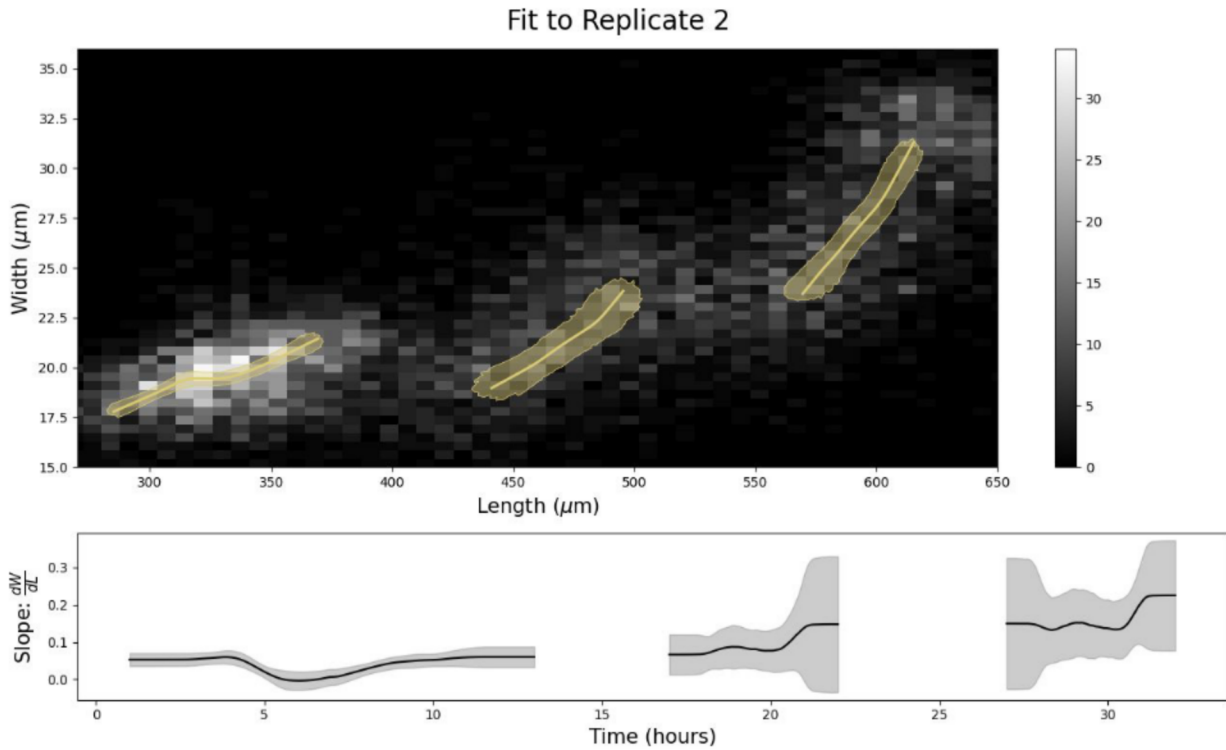
S10 Fig. Timeline of Food Utilization and Stretcher events

In the first row (grey and white) we mark the slopes determined in the Stretcher model. Transition from lighter to darker grey indicates a step increase in slope corresponding to a stiffening cuticle in the length direction. White regions denote time between larval stages. L2 and L3 are the only stages at which we have useful slope information due to the dauer decision in L1 making transitions difficult to determine and the high level of population desynchronization in L4. In the second row (green, red, and white) we mark the food and growth correlations found in (Fig 5B). Green corresponds to times at which both growth rate and food rate are increasing. Red corresponds to times at which both growth rate and food rate are decreasing. White corresponds to times at which growth rate and food rate are uncorrelated. Transitions from green to red regions occur at roughly the same times as the transition to a stiffer cuticle in the length direction.



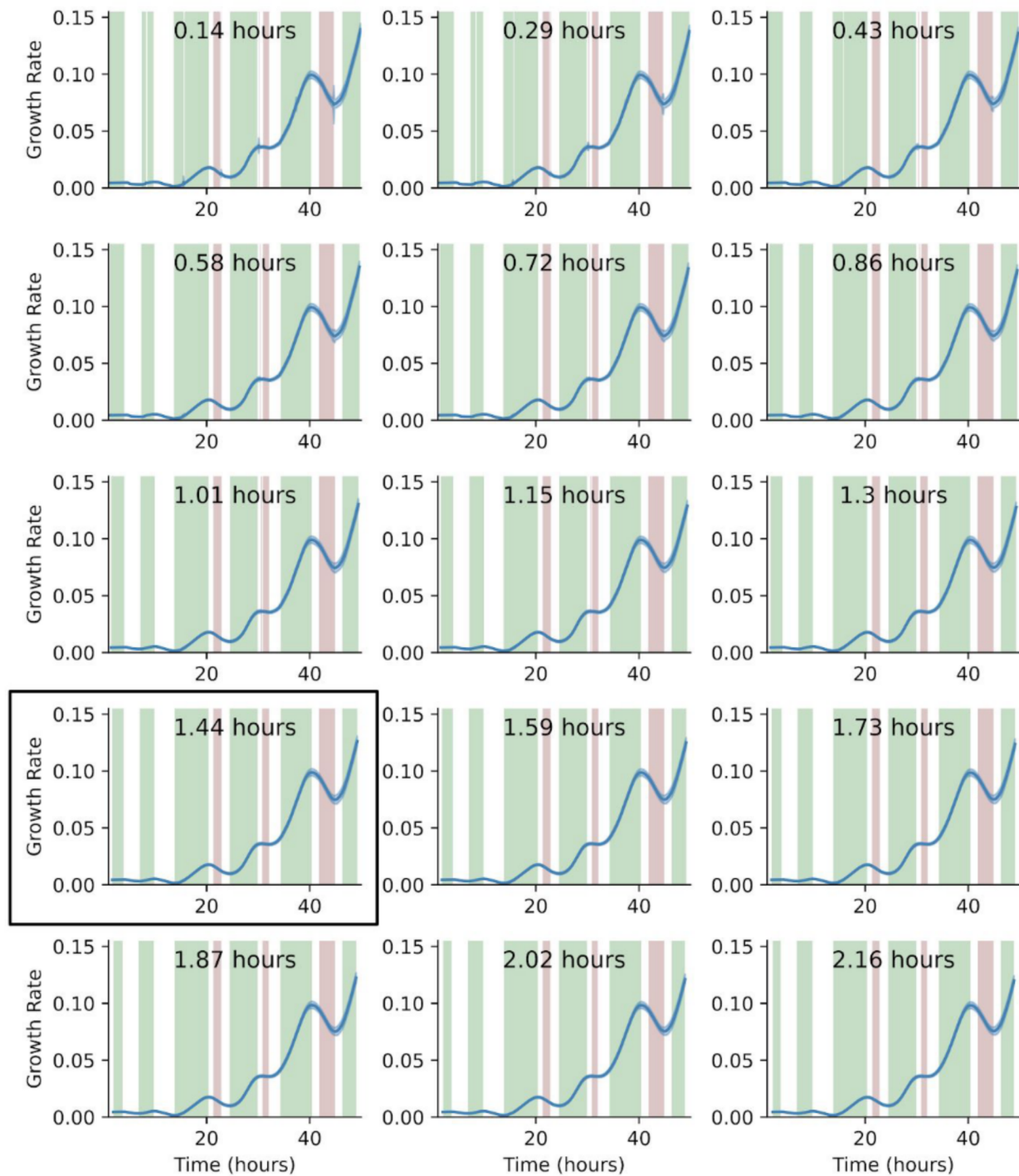
S11 Fig. Analysis of Food intake and growth rate correlation for all replicates

Summary of analysis in Fig 8 for all replicates. Until larval stage L4, most replicates follow the same pattern of transitions from one growth regime to the next. The time delay at transitions in later replicates can be explained by the temperature gradient and differences in growth between replicates.



S12 Fig. Stretcher model analysis of replicate 2 COPAS BIOSORT data for different stage thresholding

Compare to Fig 5. Larval hours defined by taking the ceiling of the lower boundary and the floor of the upper boundary. This rounding method for larval stage definition demonstrates the sensitivity of the analysis to edge effects. The unexpected step in the L2 larval stage (Fig 5) is significantly reduced with this rounding method.



S13 Fig. Sensitivity analysis to moving average window size.

Varying lengths of window sizes (0.14 to 2.16 hours) were calculated for the *lokern* growth rate regression. Window size was increased until the growth rate regression was smoothed. A window size of 1.44 hours (or 0.72 hours on either side of each time point) was chosen to calculate the start and end times of each regime (Fig 8). Continued increase of window size past 1.44 hours did not change the pattern of regimes or their boundaries significantly.

¹ Model Derivations

² Bootstrapping Algorithm

³ To calculate a robust regression of the measured COPAS BIOSORT data we bootstrap the regression using
⁴ case-resampling (Davison and Hinkley 1997, pages 261-266). Each iteration of the algorithm (**Algorithm**
⁵ **S1**) involves resampling the data of interest with replacement and maintaining the size of the sample. At
⁶ each iteration the lokern regression is calculated for Red, Length, and Width data. Additionally any desired
⁷ function (for example, volume, pumping frequency times pharynx fraction, or derivatives) of these regressions
⁸ is calculated at each iteration. Regressions at each iteration are saved and the mean and variance of these
⁹ regressions at each regression time point are used to determine the statistics of the regression.

Algorithm S1 Regression Bootstrapping with Case Resampling

```
Ndata = # animals in sample;  
iterations = # resamplings;  
  
for i = 0 to iterations do  
    Resample Ndata points with replacement. Collect Red, Length, Width data;  
  
    Apply lokern regression to resampled Red, Length, Width;  
  
    Calculate desired functions of Red, Length, Width regressions;  
  
    Save Red, Length, Width, and combined regressions;  
end for  
  
Calculate Standard deviation at each regression time point of saved regressions;
```

¹⁰ Derivation of eating model

¹¹ We begin by defining the instantaneous rate of food intake as a function of the flow rate of media through
¹² the buccal cavity and the cross sectional area of the buccal cavity.

$$\frac{dV_{food}}{dt} = A_{buccal} \quad (\text{S1})$$

¹³ We then make the assumption that the uptake of media fills the pharynx cavity we have

$$\frac{dV_{food}}{dt} = C \frac{dV_{pharynx}}{dt} \quad (\text{S2})$$

¹⁴ We average both sides of the equation under the assumption that the pumping period is significantly
¹⁵ shorter than the time scale of growth

$$\frac{1}{T} \int_0^T \frac{dV_{food}}{dt} dt = \frac{1}{T} \int_0^T CA_{buccal} \quad (S3)$$

¹⁶ The integral on the right hand side is the total food intake during a single pumping period.

$$\frac{1}{T} \int_0^T \frac{dV_{food}}{dt} dt = \frac{1}{T} \Delta V_{food} \quad (S4)$$

¹⁷ We then take into account that food is not transported to the gut in the same step as its uptake. Thus
¹⁸ the total food intake during a single pump can be calculated by the amount of food that fills the fully opened
¹⁹ pharynx

$$\frac{1}{T} \int_0^T \frac{dV_{food}}{dt} dt = \frac{C}{T} V_{pharynx:max} \quad (S5)$$

²⁰ We then replace the average on the right hand side with the average food intake rate over the pumping
²¹ period. For simplicity and because we will deal entirely with the average food intake rate, we do not use a
²² different notation for this average rate.

$$\frac{dV_{food}}{dt} = \frac{C}{T} V_{pharynx:max} = Cf(t)V_{pharynx:max} \quad (S6)$$

²³ 0.1 Transformation of sorter measurements to volume units

²⁴ To utilize sorter measurements and convert them to meaningful units we define a linear transformation from
²⁵ the correlation plots (S1 Fig)

$$L = a_1 TOF + b_1 \quad (S7)$$

$$W = a_2 norm.EXT + b_2. \quad (S8)$$

²⁶ Using Equations (S7) and (S8) we can approximate the volume of any object that passes through the
²⁷ sorter by the expression

$$V = \frac{\pi}{4} (a_1 TOF + b_1)(a_2 norm.EXT + b_2)^2. \quad (S9)$$

28 Defecation analysis

29 We use the defecation results found in (Liu and Thomas 1994) to determine if red fluorescent measurements
 30 can be used as a proxy for food intake rate as opposed to the instantaneous food volume in the gut. Defecation
 31 in adults happens very regularly, with a period of $T_d = 45 \pm 3s$, with $h_d = 43 \pm 10\%$ of their intestinal volume
 32 being expelled each time. The volume expelled is well mixed. Defining V_f as the current amount of food in
 33 the nematode gut. We can use conservation of mass to state that the rate of change in the amount of food
 34 in the gut is equal to the rate of food intake through eating less the defecation rate and the rate at which
 35 food volume is metabolized into cell products:

$$\frac{dV_f}{dt} = \frac{dV_f}{dt} \Big|_{eating} - \frac{dV_f}{dt} \Big|_{defecating} - \frac{dV_f}{dt} \Big|_{metabolized} \quad (S10)$$

36 Using red fluorescence as a proxy for food intake we can ignore the metabolism term as the fluorescent
 37 beads are not metabolized.

$$\frac{dV_f}{dt} = \frac{dV_f}{dt} \Big|_{eating} - \frac{dV_f}{dt} \Big|_{defecating} \quad (S11)$$

38 Equation (S11) states that the rate of change of the volume of fluorescent beads in the gut is equal to
 39 the difference between the intake of red fluorescent beads minus the defecation rate of red fluorescent beads.
 40 Using the results of (Liu and Thomas 1994) for the second term, and defining $V_{f:\max}$ as the volume of food
 41 in the gut just prior to defecation, h_d as the fraction of food expelled during a single defecation cycle, and
 42 T_d as the period of defecation. We average Equation (S11) over short time periods to remove the pumping
 43 and defecation period oscillations.

$$\frac{dV_{red:\max}}{dt} = \frac{dV_{red}}{dt} \Big|_{eating} - \frac{V_{red:\max} h_d}{T_d} \quad (S12)$$

44 On the left hand side, the instantaneous rate of the gut red fluorescence in Equation (S11) is replaced
 45 by the rate of change of the maximum or “full” gut fluorescence. The second term on the right hand side
 46 of Equation (S11) has been replaced by the average defecation rate over a cycle calculated by multiplying
 47 the full gut fluorescence by the fraction expelled and dividing by the defecation period. We solve Equation
 48 (S12) for the average eating rate.

$$\frac{dV_{red}}{dt} \Big|_{eating} = \frac{dV_{red:\max}}{dt} + \frac{V_{red:\max} h_d}{T_d} \quad (S13)$$

49 We take the local regression of the red fluorescence to determine $V_{red:\max}(t)$. This value is plugged into

50 the second term on the right hand side of Equation (S13) and its derivative is used to approximate the first
 51 term on the right hand side of Equation (S13). We take the adult values of h_d and T_d (Liu and Thomas
 52 1994) as a first approximation. Figure (S6) demonstrates a comparison of the red fluorescence and the red
 53 intake rate with defecation taken into account at the constant adult rates and quantities. We have scaled
 54 both the pink curve denoting red fluorescence and the blue curve denoting red intake rate by their maximum.
 55 This scaling allows us to see that the two curves are only a multiplicative factor apart up to error bars. This
 56 allows us to use the red measurement as a proxy for both red and food intake rates.

57 Derivation of Stretcher Model

58 We model the cuticle as a thin walled pressure vessel made of orthotropic, linear materials to capture the
 59 relationship between how much the cuticle stretches and the force applied to the cuticle. The relationship
 60 between the amount of stretch and the amount of applied pressure is described by the matrix:

$$\begin{bmatrix} \varepsilon_L \\ \varepsilon_{Circ} \end{bmatrix} = \begin{bmatrix} \frac{1}{E_L} & \frac{-v_{cl}}{E_c} \\ \frac{-v_{lc}}{E_L} & \frac{1}{E_c} \end{bmatrix} \begin{bmatrix} \sigma_L \\ \sigma_{Circ} \end{bmatrix} \quad (S14)$$

61 Here E_L and E_c are the Young's modulus in the length and circumferential direction, and v_{cl} and v_{lc}
 62 are the appropriate Poisson's ratios. These material properties can be measured experimentally. Normalized
 63 stretch, ε , is defined as the change in size normalized by the initial size of a cuticle in length (L) and
 64 circumference (Circ) (**Equations S15 - S16**). Here σ is the normalized force applied along the length and
 65 circumferential directions of the cuticle (**Equations S18 - S19**).

$$\varepsilon_L = \frac{\Delta L}{L_0} \quad (S15)$$

$$\varepsilon_{Circ} = \frac{\Delta Circ}{Circ_0} \quad (S16)$$

66 Here L_0 and $Circ_0$ are the length and circumference of the cuticle at the onset of stretch, or in other words
 67 at the start of a larval stage. Experimentally we measure width, not circumference, but the circumference
 68 of a circle is proportional to the width of the circle, so we can replace the circumference with the measured
 69 width:

$$\frac{\Delta Circ}{Circ_0} = \frac{\pi \Delta W}{\pi W_0} = \frac{\Delta W}{W_0} \quad (S17)$$

70 By approximating *C. elegans* as cylindrical, and assuming the only force working on the cuticle is isotropic

71 internal pressure, we can determine the normalized force in terms of pressure and geometric properties:

$$\sigma_L = \frac{r}{2t} \Delta p \quad (\text{S18})$$

$$\sigma_{Circ} = \frac{r}{t} \Delta p \quad (\text{S19})$$

72 Where r is the radius of the cylinder and t is the thickness of the cuticle. We can now rewrite Equation
 73 (S14) in terms of measurable quantities (length and width) by multiplying out the matrices making the
 74 appropriate substitutions.

$$\Delta L = \frac{L_0 r}{t} \left(\frac{1}{2E_L} - \frac{v_{cl}}{E_c} \right) \Delta p = a_L \Delta p \quad (\text{S20})$$

$$\Delta W = \frac{W_0 r}{t} \left(\frac{1}{E_C} - \frac{v_{lc}}{E_L} \right) \Delta p = a_W \Delta p \quad (\text{S21})$$

Here we compress the coefficients fixed by material and geometric properties into one constant

$$a_L = \frac{L_0 r}{t} \left(\frac{1}{2E_L} - \frac{v_{cl}}{E_c} \right) \quad (\text{S22})$$

$$a_W = \frac{W_0 r}{t} \left(\frac{1}{E_C} - \frac{v_{lc}}{E_L} \right) \quad (\text{S23})$$

75 Stretcher Slope Calculations

76 The Stretcher model predicts a constant ratio between stretch in width, ΔW , and stretch in length, ΔL .

77 These measures of stretch are changes in the length and width measurements over some period of time. To

78 see how the ratio of $\frac{\Delta W}{\Delta L}$ changes throughout a larval stage, we need to measure the stretch instantaneously.

79 To do this we take advantage of the derivative approximation

$$\Delta W \approx \frac{dW}{dt} \Delta t \quad (\text{S24})$$

$$\Delta L \approx \frac{dL}{dt} \Delta t \quad (\text{S25})$$

80 Equations (S24, S25) are combined in the ratio found in Equation (3) to give:

$$\frac{\Delta W}{\Delta L} \approx \frac{W'(t)}{L'(t)} \quad (\text{S26})$$

81 Here $W' = \frac{dW}{dt}$ and $L' = \frac{dL}{dt}$. We differentiate the time series from the local regressions of length and
82 width data. The ratio of derivatives gives the instantaneous stretch ratio as it changes over time. Due to
83 the numerical difficulty of calculating both derivatives and ratios with accuracy, we expect large error bars
84 for this ratio. To estimate the size of error bars we apply a first order error propagation formula to Equation
85 (S26).

$$\sigma_{Ratio}^2 \approx \left| \frac{\partial Ratio}{\partial (W')} \right|^2 \sigma_{(W')}^2 + \left| \frac{\partial Ratio}{\partial (L')} \right|^2 \sigma_{(L')}^2 + 2 \frac{\partial Ratio}{\partial (W')} \frac{\partial Ratio}{\partial (L')} \sigma_{(W')(L')} \quad (\text{S27})$$

$$\sigma_{Ratio}^2 \approx \left| \frac{1}{L'} \right|^2 \sigma_{(W')}^2 + \left| \frac{-(W')^2}{(L')^3} \right|^2 \sigma_{(L')}^2 - 2 \frac{W'}{(L')^3} \sigma_{(W')(L')} \quad (\text{S28})$$

86 The variance in Equation (S28) is calculated for each time point in the regressions of length and width.
87 We resample the data for each larval stage 2,000 times with replacement (see Methods for larval stage
88 determination). For each of these resampled sets of data, we numerically differentiate the length and width
89 regression to determine an estimate of the length and width derivatives over time. At each time point the
90 mean regression length and width derivatives are used in place of W' and L' . The covariance matrix for the
91 length and width derivatives is calculated at each time point using the 2,000 resampled regressions in the
92 bootstrap analysis and used as the variance terms in Equation (S28).